Closed-form analytical solution for the transfer matrix based on Pendry-MacKinnon discrete Maxwell's equations

Ovidiu-Zeno Lipan*
Department of Physics, Gottwald Center for the Sciences 138 UR Drive,
University of Richmond, Richmond, VA 23173, USA

Aldo De Sabata

Department of Measurements and Optical Electronics, Politehnica University of Timisoara, 300006 Timisoara, Romania (Dated: March 14, 2023)

Pendry and MacKinnon meaningful discretization of Maxwell's equations was put forward specifically as part of a finite-element numerical algorithm. By contrast with a numerical approach, in the same spirit evoked by the relationships between the difference and the differential equations, we provide an analytical solution for the transfer matrix elements generated by this discretization of Maxwell's equations. The method, valid for all modes and any non-magnetic pattern with frequency-dependent permittivities, is exemplified for a bilaminar structure. The results from hundreds of path-operators simplify to a small number of propagation channels, which transfer the electromagnetic field between input and output. A specific bilaminar device is design-optimized and used to generate a topological map from permittivities to the number of modes and very high Q-factor resonances.

PACS Numbers: 78.67.Pt, 42.25.Fx

I. INTRODUCTION

What follows came about as an overlap of a present technological need with a perennial scientific quest. The current need is represented by photonic devices based on thin laminae, be they in the form of waveguides for augmented reality [1], [2] or of frequency-selective surfaces for the 5 and 6G networks [3], of wearable applications [4] or of surface wave-mediated sensing applications [5], [6]. The perennial quest is to understand the interplay between discrete and continuous models [7], [8]. The focus on this association has varied since the 19th century, [9], piquing the interest of many in, for example, the theory of solitons [10], universality in chaos [11], [12], fractals [13]. The manifestation that interests us is the relationship between the difference and the differential equations. For example, the discrete version of the equation of Korteweg and de Vries for soliton wave motion, [14], shows a distinct asymmetric richness since it contains a series of universal properties that are not readily visible in the continuum. Particularly, the discrete form of soliton equations proposed by Hirota [15],[16] is connected with quantum integrable systems [17], [18]. It is essential to emphasize that it is not at all trivial to discretize an equation in a way that preserves the prime properties of the original continuous equation.

Pendry and MacKinnon obtained a meaningful discretization of Maxwell's equations [19] on a carefully chosen simple cubic lattice [20], by retaining the essential properties of the longitudinal modes present in the continuum. This discretization was put forward specifically

as part of a finite-element numerical algorithm [21].

By contrast with a numerical approach, in the same spirit evoked by the relationships between the difference and the differential equations, we asked the question of whether a complete analytical solution can be found to the transfer matrix of the Pendry and MacKinnon discrete Maxwell's equations.

The transfer matrix, [22], is widely used well beyond the study of the propagation of electromagnetic fields [23], [24]. Its common appearance is in the form of a 2×2 matrix, reduced to one propagation mode [25], [26],[27]. However, we are looking here for an analytical solution for the transfer matrix that is valid for any non-magnetic pattern and that has to encompass all Bloch-Floquet modes, either propagative or evanescent. As a consequence, our procedures differ from those employed in theories where the number of parameters are few and symmetries are many, [28],[29].

In the ensuing sections we derive this analytical solution and present the techniques we used, noteworthy among them being the definition of path-operators, Fig.3, and the appearance of propagation channels for the transfer of the electromagnetic field between input and output, Fig.5. This analytical solution is valid for filling the lattice's nodes with frequency-dependent non-magnetic isotropic material of any kind. We present the general solution for two laminae, although the method can be extended to additional laminae.

To be more specific, in Sections II and III we rewrite the Pendry and MacKinnon discrete version of Maxwell's equations to take shape in a tensor product of two 2dimensional linear spaces, (14) to (16) and (20) to (22). As a consequence, the electromagnetic states and the propagation operators are decomposed as a tensor product, (27). This course of action proves to be essential in

^{*} olipan@richmond.edu

simplifying a large volume of analytic computations. Sections IV and V are dedicated to the discrete dispersion relation in vacuum and to the on-shell scattering method, [30], from which a function along the z-coordinate is extracted, (39). The Bloch-Floquet periodic boundary conditions along the x and y axes, but not along z, are introduced in Section VI. The building up of the transfer matrix from its elements is covered in Section VII.

A key step towards the solution, the path-operators, is defined and discussed in Section VIII. The summation over the entire set of path-operators greatly simplifies the transfer matrix to reveal that the propagation run along a small number of channels, Section IX.

To concretize the proposed method, which hinges on path-operators and channels, we completely solve for the transfer matrix elements of a bilaminar structure. The presentation of the solution starts in Section X from a bird's eye view, and dives into the details in Sections XI and XII. The classification of the channels by the input-output polarization and the direction of propagation is summarized in Table I, Figs. 5 and 6 and Appendix B.

In Section XIII we segue into the continuum limit, and then apply it to the specific bilaminar pattern from Fig.7. The limit is in the x and y directions and it reveals that channels can be classified by a set of universal functions. It also calls for computing 2-dimensional Fourier integrals of products of these functions, each function's argument being defined by the permittivities of a lamina, Section XIII and XIV. For polygonal tessellated laminae, Section XV, these integrals can be computed in a closed form, Section XVI and XVII. The formulas contain a gauge freedom and are arranged as a sum of terms over the vertices of the tessellated polygons. These terms hold all the information about the non-magnetic materials and the geometric orientations of the structure, as can be seen in (80).

Lastly, from the formulas for the transfer matrix, an optimization procedure is devised in Section XVIII to create a dielectric bilaminar structure, Fig.7, on which Bloch-Floquet modes propagate along the laminae with large amplitudes, being evanescent in the z-direction [31]. These resonances display a series of relevant properties. One is the robustness with respect to the change of the dielectric constants, Section XIX. The resonant frequencies are located close to the zeroes of the diagonal elements of the transfer matrix. As the dielectric permittivities pass through different values, the zeroes are created or disappear allowing us to define a topological map that counts the number of resonant modes, Fig.10.

On a separate note, in Section XX and XXI we find that the same bilaminar structure, but with specifically selected dielectric constants, resonates with a very large Q-factor, Fig.19. Finally, in Section XXII, the complete analytical formula offers the possibility to obtain the Fano-Lorentz spectral line shape for a resonant mode, [32],[33], through a zero-pole approximation (96), in the complex frequency plane Fig.21.

II. DISCRETE MAXWELL'S EQUATIONS ON A LATTICE

Space is an orthogonal lattice with lattice constants a, band c on the x, y and z directions, respectively. The zaxis is singled-out as the propagation axis for the transfer matrix. The discrete space is thus viewed as a sequence of x, y-parallel planes labeled by the z-axis coordinate. The discrete position vector is $\vec{n} = (an_x, bn_y, cn_z) =$ (n_{\perp}, cn_z) , where the notation $n_{\perp} = (an_x, bn_y)$ emphasizes the decomposition of the space as a collection of planes perpendicular to the z-axis, as in [34]. If there is a preference to view the collection of planes as central, then \perp should be changed to \parallel everywhere in the paper. At each point of the lattice, the electromagnetic field is described by six components, \vec{E} and \vec{H} . The material attached to each lattice point is characterized by two discrete scalar fields which connect \vec{D} to \vec{E} and \vec{B} to H, respectively:

$$\vec{D} = \epsilon_0 \epsilon(n_\perp, cn_z) \vec{E}, \tag{1}$$

$$\vec{B} = \mu_0 \mu(n_\perp, cn_z) \vec{H}. \tag{2}$$

In the discrete electrodynamics that we are taking forward, the ∇ operator becomes a pair, (\vec{T}^E, \vec{T}^H) , of lattice operators, where $\vec{T}^E = (T_x^E(a), T_y^E(b), T_z^E(c))$ and $\vec{T}^H = (T_x^H(a), T_y^H(b), T_z^H(c))$. These discrete operators are defined by their action on a lattice scalar function $f(\vec{n})$. For the x-axis

$$T_x^E(a)f(\vec{n}) = (ia)^{-1}(f(\vec{n} + a\hat{x}) - f(\vec{n})),$$
 (3)

$$T_x^H(a)f(\vec{n}) = -(ia)^{-1}(f(\vec{n} - a\hat{x}) - f(\vec{n})). \tag{4}$$

with (y, b) and (z, c) taking place of (x, a), for the other axes. The Maxwell's equations on the lattice are

$$\vec{T}^E \times \vec{E} = \Gamma_H^{-1} \vec{H}', \tag{5}$$

$$\vec{T}^H \times \vec{H}' = \Gamma_E^{-1} \vec{E}, \tag{6}$$

where

$$\Gamma_H^{-1} = -i\omega^2 \epsilon_0 \mu_0 \mu(n_\perp, c n_z) c, \tag{7}$$

$$\Gamma_E^{-1} = -i\epsilon(n_\perp, cn_z)c^{-1},\tag{8}$$

$$\vec{H}' = i(\omega \epsilon_0 c)^{-1} \vec{H}. \tag{9}$$

Eliminating E_z and H'_z from Maxwell's equations, the propagation of the 4-dimensional vector field

$$|F(n_{\perp}, n_z)\rangle = \begin{bmatrix} E_x(n_{\perp}, cn_z) \\ E_y(n_{\perp}, cn_z) \\ H'_x(n_{\perp}, cn_z) \\ H'_y(n_{\perp}, cn_z) \end{bmatrix}$$
(10)

is carried on, as usual, by two operators. The first operator O_E , (11), advances only the E-components Fig.(1)

$$\begin{bmatrix} E_x(n_{\perp}, cn_z) \\ E_y(n_{\perp}, cn_z) \\ H'_x(n_{\perp}, cn_z) \\ H'_y(n_{\perp}, cn_z) \end{bmatrix} \xrightarrow{O_E(n_z)} \begin{bmatrix} E_x(n_{\perp}, cn_z + c) \\ E_y(n_{\perp}, cn_z + c) \\ H'_x(n_{\perp}, cn_z) \\ H'_y(n_{\perp}, cn_z) \end{bmatrix}. \tag{11}$$

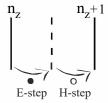


FIG. 1. Propagation between two planes. The dotted plane is fictitious and is used to place the field configuration transformed by $O_E(n_z)$. The argument n_z emphasizes that O_E depends exclusively on the material properties $\Gamma_{E/H}(n_\perp,n_z)$ on the (x,y)-plane located at n_z .

The material properties Γ_H and Γ_E embedded in the O_E matrix elements depend only on the spatial position \overrightarrow{n} located on the plane n_z . The operator O_E acts on the internal index α of the vector field F_{α} , (10), as a 4 by 4 matrix multiplication, whereas the matrix elements of O_E are operators on the external space variable n_{\perp} of the field, but not on the n_z -position. The E-step carried by O_E is followed by an H-step carried by O_H

$$\begin{bmatrix} E_x(n_{\perp}, cn_z + c) \\ E_y(n_{\perp}, cn_z + c) \\ H'_x(n_{\perp}, cn_z) \\ H'_y(n_{\perp}, cn_z) \end{bmatrix} O_H(n_z + 1) \begin{bmatrix} E_x(n_{\perp}, cn_z + c) \\ E_y(n_{\perp}, cn_z + c) \\ H'_x(n_{\perp}, cn_z + c) \\ H'_y(n_{\perp}, cn_z + c) \end{bmatrix}.$$

$$(12)$$

In contrast to O_E , the material properties Γ_H and Γ_E for the O_H matrix elements depend on the spatial position on plane n_z+1 . The complete propagation from the plane located at n_z to the one located at n_z+1 is accomplished by $O_H(n_\perp, cn_z + c)O_E(n_\perp, cn_z)$.

It is apparent from the structure of the operators O_E and O_H that the internal 4-dimensional space can be viewed as a tensor product of two 2-dimensional spaces. This decomposition proves to be efficient in classifying different paths taken by the electromagnetic propagation through materials, which will be one of our main instruments to obtain closed analytic formulas for the transfer matrix elements. So, departing from [21], the path viewpoint is expressed by writing the operators as

$$O_E(n_z) = O_E^{(1)} + O_E^{(2)} + O_E^{(3)},$$
 (13)

$$O_E^{(3)} = \mathbb{1} \otimes \mathbb{1},\tag{14}$$

$$O_F^{(2)} = I_E \otimes \sigma_2 \Gamma_H^{-1}(-c),$$
 (15)

$$O_E^{(1)} = I_E \otimes |T_E\rangle \Gamma_E \langle T_E | \sigma_2(-c), \qquad (16)$$

where σ_2 is the Pauli matrix and

$$\mathbb{1} = \begin{bmatrix} 1 & 0 \\ 0 & 1 \end{bmatrix} , I_E = \begin{bmatrix} 0 & 1 \\ 0 & 0 \end{bmatrix} , I_H = \begin{bmatrix} 0 & 0 \\ 1 & 0 \end{bmatrix}.$$
 (17)

The ket and the bra operators form (16) act on the internal space as 2-dimensional vectors and on the external

space variable n_{\perp} as operators on functions

$$|T_E\rangle = \begin{bmatrix} T_x^E \\ T_y^E \end{bmatrix} , \langle T_E| = \begin{bmatrix} T_x^H & T_y^H \end{bmatrix}.$$
 (18)

The ket to bra conjugation is defined as the change of E into H. There is no additional conjugation over the complex unit i. The labels, as is usually the case, do not change under conjugation.

Similarly, but different to the E-step, the operator for the H-step is

$$O_H(n_z+1) = O_H^{(1)} + O_H^{(2)} + O_H^{(3)}, (19)$$

$$O_H^{(3)} = 1 \otimes 1,$$
 (20)

$$O_H^{(2)} = I_H \otimes \sigma_2 \Gamma_E^{-1}(-c), \tag{21}$$

$$O_H^{(1)} = I_H \otimes |T_H\rangle \Gamma_H \langle T_H | \sigma_2(-c), \quad (22)$$

$$|T_H\rangle = \begin{bmatrix} T_x^H \\ T_y^H \end{bmatrix}, \ \langle T_H| = \begin{bmatrix} T_x^E & T_y^E \end{bmatrix}.$$
 (23)

Concordant to the tensor product decomposition of the operators, the field will be represented also as a tensor product,

$$|F(n_{\perp}, n_{z})\rangle =$$

$$|e\rangle \otimes \begin{bmatrix} E_{x}(n_{\perp}, cn_{z}) \\ E_{y}(n_{\perp}, cn_{z}) \end{bmatrix} + |h\rangle \otimes \begin{bmatrix} H'_{x}(n_{\perp}, cn_{z}) \\ H'_{y}(n_{\perp}, cn_{z}) \end{bmatrix},$$
(24)

where the 2-dimensional vectors $|e\rangle$ and $|h\rangle$,

$$|e\rangle = \begin{bmatrix} 1\\0 \end{bmatrix}, |h\rangle = \begin{bmatrix} 0\\1 \end{bmatrix}, \tag{25}$$

select the electric part (E_x, E_y) and the magnetic part (H'_x, H'_y) of the 4-dimensional vector (E_x, E_y, H'_x, H'_y) , respectively.

III. BASIS VECTORS FOR FIELDS ON A LATTICE

The solutions to Maxwell's equations on a lattice filled with a homogeneous medium, i.e. constant $\Gamma_H(n_\perp,cn_z)=\Gamma_H$ and $\Gamma_E(n_\perp,cn_z)=\Gamma_E$, are plane waves. These solutions, $\left|\Psi_{S/P,p_\perp}^{\pm}\right\rangle e^{\pm ip_zn_zc}e^{-i\omega t}$, are distinguished by the type of polarization S or P and by the direction of propagation \pm along the positive or negative z-direction. Here

$$\left|\Psi_{S/P,p_{\perp}}^{\pm}\right\rangle = \left|p_{\perp}, S/P, \pm\right\rangle e^{ip_{\perp}n_{\perp}},$$
 (26)

with the propagation in the (x, y)-plane described by $p_{\perp} = (p_x, p_y)$.

The internal 4-dimensional vectors of the plane waves are

$$|p_{\perp}, S, +\rangle = |e\rangle \otimes i\sigma_{2} |p_{\perp}^{H}\rangle + |h\rangle \otimes |p_{\perp}^{H}\rangle \Gamma_{H} k_{z}^{E}, |p_{\perp}, P, +\rangle = |e\rangle \otimes |p_{\perp}^{E}\rangle \Gamma_{E} k_{z}^{H} + |h\rangle \otimes i\sigma_{2} |p_{\perp}^{E}\rangle,$$
(27)

where, consistent with (18) and (23), the column vectors $|p_{\perp}^{E}\rangle$ and $|p_{\perp}^{H}\rangle$ are the transpose and $E \rightleftharpoons H$ conjugate of the row vectors $\langle p_{\perp}^{E}| = [k_{x}^{H}, k_{y}^{H}]$ and $\langle p_{\perp}^{H}| = [k_{x}^{E}, k_{y}^{E}]$, respectively. The space being discrete, the plane wave depends on the lattice constants (a, b, c) through the vectors $\overrightarrow{k}^{E} = (k_{x}^{E}, k_{y}^{E}, k_{z}^{E})$ and $\overrightarrow{k}^{H} = (k_{x}^{H}, k_{y}^{H}, k_{z}^{H})$,

$$k_x^E = (ia)^{-1}(e^{iap_x} - 1),$$
 (28)

$$k_x^H = -(ia)^{-1}(e^{-iap_x} - 1),$$
 (29)

with the pairs (b, p_y) and (c, p_z) instead of (a, p_x) , for the other axes. To obtain the other two basis vectors, $|p_{\perp}, S/P, -\rangle$, change k_z^E from $|p_{\perp}, S/P, +\rangle$ into $-k_z^H$.

To derive the transfer matrix elements, the field (24), at a given n_z , is decomposed in the basis $\left|\Psi_{S/P,p_{\perp}}^{\pm}\right\rangle$. The decomposition is carried out by projecting on an orthogonal set of bra vectors (30)

$$\left\langle \Phi_{S/P,p_{\perp}}^{\pm} \right| = \left\langle p_{\perp}, S/P, \pm \right| e^{-ip_{\perp}n_{\perp}}, \tag{30}$$

where

$$\langle p_{\perp}, S, + | = -\langle e | \otimes \langle p_{\perp}^{H} | i\sigma_{2}k_{z}^{H} + \langle h | \otimes \langle p_{\perp}^{H} | \Gamma_{H}^{-1}, \langle p_{\perp}, P, + | = \langle e | \otimes \langle p_{\perp}^{F} | \Gamma_{E}^{-1} - \langle h | \otimes \langle p_{\perp}^{F} | i\sigma_{2}k_{z}^{E}.$$
(31)

Multiply $\langle p_{\perp}, S/P, +|$ by -1 and change k_z^H into $-k_z^E$ to attain $\langle p_{\perp}, S/P, -|$. The orthogonal basis is not normalized. The norm, $\langle p_{\perp}^H | p_{\perp}^H \rangle (k_z^H + k_z^E) = \langle p_{\perp}^E | p_{\perp}^E \rangle (k_z^E + k_z^H)$, is invariant to $E \leftrightarrows H$ conjugation.

IV. DISPERSION RELATION FOR A HOMOGENEOUS MEDIUM

The requirement that the plane wave basis satisfy Maxwell's equations on the lattice filled with a homogeneous medium imposes that

$$-(\Gamma_H \Gamma_E)^{-1} = \langle p_\perp^H | p_\perp^H \rangle + k_z^E k_z^H. \tag{32}$$

This is the dispersion relation for the homogeneous medium

$$\frac{\omega^2}{v_0^2} = k_x^E k_x^H + k_y^E k_y^H + k_z^E k_z^H, \tag{33}$$

where the velocity of light in that medium is v_0 . Through the following c-scaling

$$\frac{\omega}{v_0} = \frac{\Omega}{c} = \frac{2\pi}{\lambda},\tag{34}$$

the dispersion relation is written in terms of a unitless frequency Ω

$$\frac{\Omega^2}{c^2} = k_x^E k_x^H + k_y^E k_y^H + k_z^E k_z^H, \tag{35}$$

which will become useful for expressing the transfer matrix elements in terms of unitless parameters. Note that the term $k_x^E k_x^H + k_y^E k_y^H$, which is equal to $\langle p_\perp^E | p_\perp^E \rangle = \langle p_\perp^H | p_\perp^H \rangle$, tends in the continuum limit $a \to 0, b \to 0$ to $p_x^2 + p_y^2$. In what follows, we use vacuum as the homogeneous medium for the basis. Interchangeably, this medium will be called also as the reference medium for the basis.

V. SOLVING FOR $\varphi_z = e^{icp_z}$ FOR GIVEN Ω , p_x AND p_y

The approach in [19] is to work on-shell which means solve the dispersion relation for p_z , given the frequency Ω and p_{\perp} . To this end, we introduce the function φ_z

$$\varphi_z = e^{icp_z},\tag{36}$$

which is the solution to the equation

$$\varphi_z + \varphi_z^{-1} = 2\zeta, \tag{37}$$

where

$$\zeta = 1 - \frac{\Omega^2}{2} + \frac{c^2}{2} \left\langle p_{\perp}^{\mathrm{H}} \middle| p_{\perp}^{\mathrm{H}} \right\rangle. \tag{38}$$

There are two distinct and non-overlapping constraints that we impose on p_z from (36). One condition is $\operatorname{Im}(p_z) \geqslant 0$ so that evanescent waves generated away from sources placed at $z = -\infty$ or at $z = \infty$ are represented by a decaying φ_z or φ_z^{-1} , respectively. The other condition is $p_z \geqslant 0$ enforcing the velocity of propagating waves coming from $z = -\infty$ or $z = \infty$ to be oriented along \hat{z} or $-\hat{z}$, respectively. The formal solution to the equation (37), $\varphi_z = \zeta \pm \sqrt{\zeta^2 - 1}$ divides the real axis into three intervals, $(-\infty, -1)$, (-1, 1) and $(1, \infty)$. The requirement $\operatorname{Im}(p_z) \geq 0$ for the interval $(-\infty, -1)$ selects the $\varphi_z = \zeta - \sqrt{\zeta^2 - 1}$ but does not impose specific values for φ_z on $(-\infty, -1)$. Both walks in the ζ -complex plane above or below $(-\infty, -1)$ satisfy $\operatorname{Im}(p_z) \geq 0$. The second constrain, $p_z \ge 0$, requires the values of φ_z on (-1,1)to be those obtained from walking below the segment (-1,1). For the last interval the constrain $\text{Im}(p_z) \ge 0$ is fulfilled and, like for $(-\infty, -1)$, we are free to define φ_z on $(1,\infty)$ from walking above or below the interval. We opt to construct a function φ_z continuous from below, $\operatorname{Im}(\zeta) \leq 0$, and so select the values of φ_z on the real axis by walking below it in the ζ -complex plane.

This analysis leads to the following solution

$$\varphi_z(\zeta) = \zeta - \sqrt{|\zeta^2 - 1|} e^{\frac{i}{2} \left(\arg(\zeta - 1) + \arg(\zeta + 1)\right)}.$$
 (39)

The $arg(\zeta)$ takes values on $[-\pi,\pi)$ in such a way that $\arg(\zeta) = -\pi$ if $\operatorname{Im}(\zeta) = 0$ and $\zeta < 0$. In Fig.2 the point $\varphi_z = 1$ defines the Rayleigh frequency, at which, for a given p_{\perp} , the waves turn from evanescent to propagating.

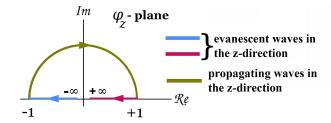


FIG. 2. The complex plane of φ_z . As ζ variable runs from $-\infty$ to -1, φ_z goes from 0 to -1. Then, as ζ runs from -1 to 1 below the real ζ -axis, φ_z follows the upper semicircle from -1 to 1. Finally, the variable φ_z moves back toward 0 from 1 as ζ covers the range from 1 to ∞ .

PERIODIC BOUNDARY CONDITIONS

Consider that the electromagnetic field is subjected to the Bloch-Floquet boundary conditions

$$|F(n_{\perp} + (a,0)L_x, cn_z)\rangle = e^{2\pi i \xi_x} |F(n_{\perp}, cn_z)\rangle, \quad (40)$$

$$|F(n_{\perp} + (0,b)L_y, cn_z)\rangle = e^{2\pi i \xi_y} |F(n_{\perp}, cn_z)\rangle, \quad (41)$$

where $L_x \ge 2$ and $L_y \ge 2$ are two integer numbers selected to describe the dimensions of a unit cell in the (x,y)-plane. The material properties are taken to be periodic from one unit cell to another

$$\Gamma_H(n_\perp + (a,0)L_x, n_z) = \Gamma_H(n_\perp, n_z) \tag{42}$$

$$\Gamma_H(n_{\perp} + (0, b)L_y, n_z) = \Gamma_H(n_{\perp}, n_z) \tag{43}$$

with a similar periodicity for Γ_E . The Bloch-Floquet boundary condition reduces the possible values for (p_x, p_y) to

$$p_x = 2\pi \frac{M_x}{aL_x} + 2\pi \frac{\xi_x}{aL_x},\tag{44}$$

$$p_{y} = 2\pi \frac{M_{y}}{bL_{y}} + 2\pi \frac{\xi_{y}}{bL_{y}},\tag{45}$$

where $M_x = 0, 1, \dots, L_x - 1$ and $M_y = 0, 1, \dots, L_y - 1$,

with $0 \le \xi_x < 1$, $0 \le \xi_y < 1$. The indices of the basis, written as $|\psi_{\text{PQL,BF}}^{\text{DIR}}\rangle$, are thus of four categories. The first, POL, is the polarization index, which takes two values S and P. The second, DIR, is the direction of propagation of the plane wave along the z-axis, which also take two values, + and -. The third, BF, is the Bloch-Floquet index consisting of pairs of integer numbers (M_x, M_y) and it takes a finite number of values. The last index, (ξ_x, ξ_y) takes only one value and can be viewed as a label for the entire Bloch-Floquet linear basis.

The parameters (ξ_x, ξ_y) specify the direction of the wave in the (x, y)-plane. For example, if the direction of the incoming mode $(M_x = 0, M_y = 0)$ is stated in spherical coordinates by the angles (θ, φ) , then the parameterization of ξ_x and ξ_y is

$$\sin\left(\pi \frac{\xi_x}{L_x}\right) = \frac{a\Omega}{2c}\sin(\theta)\cos(\varphi),\tag{46}$$

$$\sin\left(\pi \frac{\xi_y}{L_y}\right) = \frac{b\Omega}{2c}\sin(\theta)\sin(\varphi),\tag{47}$$

$$\sin\left(\frac{1}{2}cp_z\right) = \frac{c\Omega}{2c}\cos(\theta). \tag{48}$$

The first two equations give ξ_x, ξ_y for chosen θ, φ and Ω , whereas the third equation solves for p_z .

TRANSFER AND SCATTERING MATRICES

To go ahead and propagate from the IN plane located at n_z to the OUT at $n_z + L_z$, decompose the IN and OUT fields in the plane wave basis, (26), labeled as $\left|\psi_{\text{pol,bf}}^{\text{dir}}\right\rangle$ and $|\psi_{\text{POL,BF}}^{\text{DIR}}\rangle$, respectively. The z-phases, $e^{\pm ip_z^{\text{IR}}n_z}$ and $e^{\pm ip_z^{OUT}(n_z+L_z)}$, which are not included in the basis, are generated by the operators and so they do appear in the transfer matrix elements. The transfer matrix elements are defined in (49) as the factors that connect the coefficients of the $|F^{\text{IN}}(n_{\perp}, n_z)\rangle$ and $|F^{\text{OUT}}(n_{\perp}, n_z + L_z)\rangle$ fields decomposed in the reference medium plane wave basis

$$C_{\mathrm{POL,BF}}^{\mathrm{DIR}} = \sum \left(T_{\mathrm{POL,BF;pol,bf}}^{\mathrm{DIR;dir}} \right) C_{\mathrm{pol,bf}}^{\mathrm{dir}} ,$$
 (49)

the sum being over indices (dir.pol.bf) related to the IN parameters. The transfer matrix elements T in (49) borrow, from the basis, all four index categories. Building a matrix out of the T-coefficients of (49) requires a map from the 2-dimensional Bloch-Floquet index (M_x, M_y) to a 1-dimensional integer index $m = 1, 2, \dots, L_x L_y$. We use the Rayleigh frequency of (M_x, M_y) to both map and order the Bloch-Floquet index. If the Rayleigh frequency of (M_x, M_y) is less than the Rayleigh frequency of (M'_x, M'_y) we order the Bloch-Floquet indices as $(M_x, M_y) < (M'_x, M'_y)$. If two distinct Bloch-Floquet modes have the same Rayleigh frequency, the order used is the lexicographic order. Note that this ordering depends on (ξ_x, ξ_y) . The mode $(M_x, M_y) = (0,0)$ has $f_{\text{Rayleigh}} = 0$ and it is mapped into m = 1. The next $f_{\text{Rayleigh}} > 0$ is mapped into m = 2 and so on TableXII from Appendix I.

The process of building the transfer matrix out of its elements starts with all 2×2 matrices

$$T_{m,n}^{-,-} = \begin{pmatrix} T_{Sm,Sn}^{-,-} & T_{Sm,Pn}^{-,-} \\ T_{Pm,Sn}^{-,-} & T_{Pm,Pn}^{-,-} \end{pmatrix}$$
 (50)

constructed for each pair (m, n). These matrices contain the information about the transfer, through the device, of the mode n with a negative direction present at IN into the mode m, also with a negative direction but located at OUT.

From these 2×2 -matrices, construct the transfer matrix $T^{-,-}$ by letting the Bloch-Floquet indices m and n run from 1 to L_xL_y

$$T^{-,-} = \begin{pmatrix} T_{1,1}^{-,-} & T_{1,2}^{-,-} & T_{1,3}^{-,-} & \cdots \\ T_{2,1}^{-,-} & T_{2,2}^{-,-} & T_{2,3}^{-,-} & \cdots \\ T_{3,1}^{-,-} & T_{3,2}^{-,-} & T_{3,3}^{-,-} & \cdots \\ \cdots & \cdots & \cdots \end{pmatrix}.$$
 (51)

Once all four matrices $T^{-,-}, T^{-,+}, T^{+,-}, T^{+,+}$ are constructed in a similar manner, the complete transfer matrix appears as

$$T(\xi_x, \xi_y) = \begin{pmatrix} T^{+,+} & T^{+,-} \\ T^{-,+} & T^{-,-} \end{pmatrix},$$
 (52)

where (ξ_x, ξ_y) are explicitly written here to remind us of their role.

The elements of the scattering matrix can now be obtained from the complete transfer matrix. The input and output have a different meaning for the scattering matrix than OUT and IN have for the transfer matrix. Instead of "DIR/dir", for the scattering matrix we use a position index, which is either min or max depending on the position on the z-axis of the field $|F\rangle$, at $z=n_z$ or at $z=n_z+L_z$, respectively. The polarization and the Bloch-Floquet indices remain the same.

The well-known procedure to obtain the scattering matrix, [20],

$$t(\xi_x, \xi_y) = \begin{pmatrix} t^{max,min} & t^{max,max} \\ t^{min,min} & t^{min,max} \end{pmatrix},$$
 (53)

requires the inverse of the transfer matrix $T^{-,-}$

$$t^{min,max} = (T^{-,-})^{-1}, (54)$$

$$t^{min,min} = -t^{min,max}T^{-,+}, (55)$$

$$t^{max,max} = T^{+,-}t^{min,max}, (56)$$

$$t^{max,min} = T^{+,+} + t^{max,max}T^{-,-}t^{min,min}.$$
 (57)

VIII. PROPAGATION BY PATH-OPERATORS

The transfer matrix elements (49) can be written in terms of the propagation operator

$$T_{\text{POL,BF; pol,bf}}^{\text{DIR; dir}} = \|\text{OUT}\|^{-1} (L_x L_y)^{-1} \sum_{n_{\perp}} (58)$$
$$\langle \phi_{\text{POL,BF}}^{\text{DIR}} | \text{Operator } |\psi_{\text{pol,bf}}^{\text{dir}} \rangle,$$

where the normalization in the internal space and the Operator are

$$\|\text{OUT}\| = \left\langle p_{\perp}^{H,\text{OUT}} \middle| p_{\perp}^{H,\text{OUT}} \right\rangle \left(k_z^{H,\text{OUT}} + k_z^{E,\text{OUT}} \right), \quad (59)$$

$$\text{Operator} = O_H(n_z + L_z) O_E(n_z + L_z - 1) \qquad (60)$$

$$\dots O_H(n_z + 1) O_E(n_z).$$

The common approach, also followed by [20], is to place the resolution of identity between every pair of O_HO_E operators in the product (60). Within this procedure, for a stack of laminae we need to multiply a set of large-dimensional transfer matrices, one for each lamina. This implies that to grasp one desired transfer matrix element of the stack we actually need to compute all elements, which can be computationally taxing, at both levels, theoretical or numerical. Furthermore, the advantage of using a sequence of matrix products is diminished by numerical instabilities and, potentially, by approximating a large-dimensional transfer matrix by a smaller one.

To avoid using products of matrices we develop a different procedure, which, to the best of our knowledge is new in the context of transfer matrices for non-homogeneous permittivity and permeability materials.

To exemplify, consider $\left|\psi_{\mathrm{pol,bf}}^{\mathrm{dir}}\right\rangle = \left|p_{\perp}^{\mathrm{IN}}, S, +\right\rangle e^{ip_{\perp}^{\mathrm{IN}}n_{\perp}}$ at IN and $\left\langle\phi_{\mathrm{POL,BF}}^{\mathrm{DIR}}\right| = \left\langle p_{\perp}^{\mathrm{OUT}}, S, +\right| e^{-ip_{\perp}^{\mathrm{OUT}}n_{\perp}}$ at OUT in (58). There are several decisive moments in this manuscript. One is here, where we decide to expand the product operator as a sum of path-operators. Namely, since each O_E and O_H is a sum of there operators, (13) and (19), (60) becomes a sum of 3^{L_z+1} terms $O_H^{(j)}O_E^{(k)}\dots O_H^{(m)}O_E^{(n)}$, parameterized by a path (IN n,m,\ldots,k,j OUT), where each index takes three values. Each path can be represented graphically, like in Fig.3, by associating a $j \bullet$ and a $j \circ$ to $O_E^{(j)}$ and $O_H^{(j)}$, respectively. For example, the path-operator $O_H^{(j)}O_E^{(3)}O_H^{(2)}O_E^{(1)}O_H^{(2)}O_E^{(1)}$ for the path IN121232OUT is represented in Fig.3

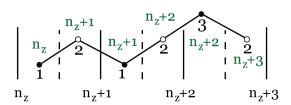


FIG. 3. One possible path for a $L_z = 3$ propagation. The path is IN121232OUT, labeled following the positive z-axis.

IX. CHANNELS

The transfer matrix element is thus a sum over pathoperators

$$\|\text{OUT}\|^{-1} (L_x L_y)^{-1} \sum_{paths} \sum_{n_{\perp}} e^{-ip_{\perp}^{\text{OUT}} n_{\perp}}$$

$$\langle p_{\perp}^{\text{OUT}}, S, +| \text{ path-operator } | p_{\perp}^{\text{IN}}, S, + \rangle e^{ip_{\perp}^{\text{IN}} n_{\perp}}.$$

$$(61)$$

We continue with the chosen example where S+ is placed at both IN and OUT. However, the liberty of choos-

ing any pair of polarization and direction at both IN

and, independently, OUT, is manifestly visible in (61). To proceed further, the tensor product decomposition of both the basis and the operators proves to be very useful. Each element of the basis, (27), is a sum of two parts, the e-part and the h-part, that contains $|e\rangle$ and $|h\rangle$, respectively. The same kind of decomposition is valid for the path-operator, where there is an I_E -part and an I_H -part in (13) and (19). Due to these decompositions, the tensor product in $\langle p_{\perp}^{\text{OUT}}, S, +|$ path-operator $|p_{\perp}^{\text{IN}}, S, +\rangle$ splits as a product of two factors. The first factor is of the form $\langle e|I_HI_EI_2I_HI_1\cdots I_E|h\rangle$, and alike versions. It can take only two values, 0 or 1. For each non-zero path that survives this first-factor selection, we must compute the second factor, which contains the material properties. For this paper we confine ourselves to non-magnetic materials.

The structure of the second factor is of the form $\left\langle p_{\perp}^{H,\mathrm{OUT}} \middle| T_E \right\rangle \Gamma_P \sigma_2 \cdots \middle| p_{\perp}^{E,\mathrm{IN}} \right\rangle$, which, drawing on $\left\langle T_E \middle| \sigma_2 \middle| T_H \right\rangle e^{ip_{\perp} \cdot n_{\perp}} = 0$, offers a second zero-selection procedure. Moreover, the second factor, for those paths that are overall non-zero, admits, as well, a pleasing and advantageous factorization into two terms. One term, call it the \mathcal{Z} -term, is a function of $(p_z^{\mathrm{IN}}, p_z^{\mathrm{OUT}}, \Omega)$ but not on the materials parameters, whereas the other, call it the XY-term, depends on p_{\perp}^{IN} and the deposited materials. This factorization is crucial in simplifying the final result for the transfer matrix because, fortunately, the XY-term is common to a group of paths.

We will call a channel a subset of paths, which have the same XY-term. The main significance is that the number of channels is much smaller than the number of non-zero paths, substantially reducing the final analytical expression for a transfer matrix element. Furthermore, the \mathcal{Z} -term of a channel, which is the sum of the \mathcal{Z} -terms of the paths that belong to that channel, simplifies into products of φ_z -dependent factors.

The technique to separate a \mathcal{Z} -term from an XY-term is to forward-propagate the input phase $e^{ip_{\perp}^{\text{IN}} \cdot n_{\perp}}$ and backward-propagate the output phase $e^{ip_{\perp}^{\text{IN}} \cdot n_{\perp}}$, both through the chain of path-operator product. These propagations are carried through the path-operator by using the general relation

$$\sum_{n_{\perp}} e^{-ip_{\perp}^{\text{OUT}} \cdot n_{\perp}} f_{\text{OUT}}(n_{\perp}) \left(\left| T_{E/H} \right\rangle (f_{\text{IN}}(n_{\perp}) e^{ip_{\perp}^{\text{IN}} \cdot n_{\perp}}) \right) =$$

$$\sum_{n_{\perp}} \left(-\left| T_{H/E} \right\rangle (e^{-ip_{\perp}^{\text{OUT}} \cdot n_{\perp}} f_{\text{OUT}}(n_{\perp})) \right) f_{\text{IN}}(n_{\perp}) e^{ip_{\perp}^{\text{IN}} \cdot n_{\perp}}.$$
(62)

For the specific aim of splitting-up the \mathcal{Z} from the XY-factor, the forward-propagation proceeds as long as $f_{\rm IN}(n_{\perp})$ is a constant independent of n_{\perp} . With or without the use of (62), a trivial observation is that the phase $e^{ip_{\perp}^{\rm IN}}$ can be pushed through $|T_E\rangle$ leaving behind $|p_E^{\rm IN}\rangle$. However, (62) brings in clarity for the backward-propagation. In this case, i.e. for constant $f_{\rm OUT}(n_{\perp})$,

the phase $e^{-ip_{\perp}^{\text{OUT}}}$ is acted upon by $-|T_H\rangle$, creating $|p_E^{\text{OUT}}\rangle$, but at the output. The splitting-up procedure stops when each phase meets its own n_{\perp} -dependent nonmagnetic materials. The sub-chain of a path-operator that extends between the final propagation positions of $e^{-ip_{\perp}^{\text{OUT}}\cdot n_{\perp}}$ and $e^{ip_{\perp}^{\text{IN}}\cdot n_{\perp}}$ is the XY-operator, which defines a channel. Once the classification of channels is at hand, the complete solution for the transfer matrix elements is obtained by continuing the forward-propagation of the phase $e^{ip_{\perp}^{\text{IN}}}$, but now through the non-magnetic material-dependent XY-operators. We explain this below, solving the case of a structure composed of two nonhomogeneous non-magnetic laminae.

X. ANALYTICAL SOLUTION FOR A BILAMINAR NON-MAGNETIC STRUCTURE

It is not difficult to complete the path-operator calculation for a single lamina carrying an (n_x, n_y) -dependent non-magnetic materials. The next in line is a bilaminar structure, which gives rise to a greater range of scattering phenomena. Although its complete solution may seem arduous, the end result elucidates the role played by each propagation channel. Furthermore, the analytical solution combined with optimization procedures provides a method for designing practical devices, Section XVIII.

In what follows we present the solution to the pathoperator propagation for a device composed of two laminae with non-homogeneous and distinct non-magnetic materials $\epsilon_1(n_x, n_y) \neq \epsilon_2(n_x, n_y)$, Fig.4.

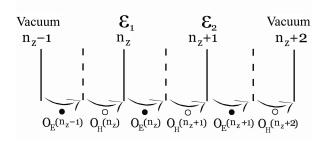


FIG. 4. Propagation from vacuum through two thin laminae, back into the vacuum. Planes 1 and 2, printed with nonhomogeneous $\epsilon_1(n_{\perp})$ and $\epsilon_2(n_{\perp})$, form laminae 1 and 2, respectively.

First we take an overall view of the results, followed by an in-depth study of propagation through path-operators.

From the total of $3^6 = 729$ paths only 188 paths, counted for all possible polarization pairs, are non-zero. These paths are grouped into channels. The channels through which the plane waves propagate from IN at $n_z - 1$ to OUT at $n_z + 2$, depend on the polarization index, Tab.I. For example, the specific propagation from S^{IN} into S^{OUT} goes through 104 paths, the contributions from the rest of the paths, up to 188, being zero

for this polarization pair. These 104 paths are grouped in 5 channels Tab.I. Channel 1 of $S^{OUT}S^{IN}$ contains 46 paths, Channel 2 comprises 22 and so on, until Channel 5, which is built on 20 paths. Tab.I contains, for each pair of IN-OUT polarization, the information for the number of channels and the number of paths per channel.

TABLE I. Channels

$Pol^{OUT}Pol^{C}$	No. of paths per channel
$S^{OUT}S^{IN}$	104=46+22+8+8+20
$S^{OUT}P^{IN}$	77=33+16+4+12+12
$P^{OUT}S^{IN}$	63 = 4 + 4 + 4 + 4 + 10 + 10 + 6 + 6 + 15
$P^{OUT}P^{IN}$	96 = 10 + 2 + 6 + 2 + 6 + 8 + 2 + 6 + 6 + 15 + 12 + 3 + 9 + 9

^a The number of channels, from the second column, are: 5,5,9 and 14.

By way of example, to justify these results, and more, we will analyze three paths.

TABLE II. Channel 3 SS

paths	paths
IN221221OUT	IN321221OUT
IN221222OUT	IN321222OUT
IN221223OUT	IN321223OUT
IN221233OUT	IN321233OUT

 $^{^{\}rm a}$ The common sequence 212 defines the XY-operator for this channel

Two paths are selected form the 729-188 set of zeropaths to explain the source of their null contribution to propagation.

The path IN321321OUT does not contribute at all to any polarization propagation because the operator product for this path, $O_H^{(1)}O_E^{(2)}O_H^{(3)}O_E^{(1)}O_H^{(2)}O_E^{(3)}$, is of the form $(I_HI_E1_II_EI_H1)\otimes$ (operator). The part $I_E1_II_E=|e\rangle\langle h|1|e\rangle\langle h|$ is zero, since $\langle h|e\rangle=0$, which renders the paths inactive to any propagation.

Another path, IN321121OUT is also zero, but for a different reason. Its path-operator $O_H^{(1)}O_E^{(2)}O_H^{(1)}O_E^{(2)}O_H^{(2)}O_E^{(3)}$ is of the form $(I_HI_EI_HI_EI_H\mathbbm{1})\otimes (\text{operator})$. The first term of the tensor product, $(I_HI_EI_HI_EI_H\mathbbm{1})=|h\rangle\langle e|$, is not zero. However, the second term of its tensor product contains $O_H^{(1)}O_E^{(1)}=|T_H\rangle\,\Gamma_S\,\langle T_H|\,\sigma_2(-c)\,|T_E\rangle\,(-c\Gamma_P)\,\langle T_E|\,\sigma_2$. This brings into contact $\langle T_H|$ with $|T_E\rangle$ acted by σ_2 , which is zero

$$\begin{bmatrix} T_x^E \\ T_y^E \end{bmatrix} \sigma_2 \begin{bmatrix} T_x^E & T_y^E \end{bmatrix} = i(T_y^E T_x^E - T_x^E T_y^E) = 0, \quad (63)$$

given that T_y^E and T_x^E commute. We are left with the propagation along 188 non-zero paths, which is exemplified next.

XI. CHANNEL 3 SS

Compute the contribution of the path IN321221OUT to the propagation of $S^{\text{IN},+}$ into $S^{\text{OUT},+}$. This path is part of Channel 3 $S^{\text{OUT}}S^{\text{IN}}$, which contains 8 paths, Tab.II. Its path-operator is of the form $|h\rangle \langle e| \otimes$ (operator). To evaluate its contribution to the transfer matrix element, the operator needs to act on both the input $|p_{\perp}^{\text{IN}}, S, +\rangle e^{ip_{\perp}^{\text{IN}}n_{\perp}}$ and on the output $e^{-ip_{\perp}^{\text{OUT}}n_{\perp}} \langle p_{\perp}^{\text{OUT}}, S, +|$, (61). The first term $|h\rangle \langle e|$ tells us that only the e-part of the input $|p_{\perp}^{\text{IN}}, S, +\rangle$ is delivered, by this path, into the h-part of the output $\langle p_{\perp}^{\text{OUT}}, S, +|$.

Use, for a non-magnetic device, $\Gamma_H^{-1}=\Omega^2(ic)^{-1}$ and $\Gamma_E^{-1}=i\epsilon(n_\perp)c^{-1}$ to arrive at

$$\|\text{OUT}\|^{-1} (L_x L_y)^{-1} \sum_{n_{\perp}} e^{-ip_{\perp}^{\text{OUT}} n_{\perp}}$$
 (64)

$$ic^{3}\Omega^{2}\left\langle p_{\perp}^{\mathrm{OUT,H}}\middle|T_{H}\right\rangle\left\langle T_{H}\middle|\sigma_{2}\epsilon_{2}\middle|T_{E}\right\rangle\epsilon_{1}^{-1}\left\langle T_{E}\middle|\epsilon_{1}\sigma_{2}\middle|p_{\perp}^{\mathrm{IN,H}}\right\rangle$$

$$e^{ip_{\perp}^{\mathrm{IN}}n_{\perp}}.$$

Factorize the summand into a \mathcal{Z} -factor and an XY-factor, by back-propagating $e^{-ip_{\perp}^{\text{OUT}}n_{\perp}}$ through $|T_H\rangle$ at OUT, (62), whereas at IN use $|T_H\rangle e^{ip_{\perp}^{\text{IN}}n_{\perp}} = \left|p_{\perp}^{\text{IN},\text{H}}\rangle e^{ip_{\perp}^{\text{IN}}n_{\perp}}$,

$$\|\mathrm{OUT}\|^{-1} (L_x L_y)^{-1} \sum_{n_\perp} e^{-ip_\perp^{\mathrm{OUT}} n_\perp} i c^3 \Omega^2 \left\langle p_\perp^{\mathrm{OUT,H}} \middle| p_\perp^{\mathrm{OUT,H}} \right\rangle$$

$$\langle T_H | \sigma_2 \epsilon_2 | T_E \rangle \epsilon_1^{-1} \langle T_E | \epsilon_1 \sigma_2 | T_H \rangle e^{i p_{\perp}^{\text{IN}} n_{\perp}}.$$
 (65)

For this path, the \mathcal{Z} -factor is $ic^3\Omega^2 \left\langle p_\perp^{\mathrm{OUT,H}} \middle| p_\perp^{\mathrm{OUT,H}} \right\rangle$. For other paths, both variables φ_z^{OUT} and φ_z^{IN} are present in the result.

The XY-operator, which is common to all 8 paths from channel₃-SS and thus defines this channel, is

Operator-
$$XY_3^{SS} = \langle T_H | \sigma_2 \epsilon_2 | T_E \rangle \epsilon_1^{-1} \langle T_E | \epsilon_1 \sigma_2 | T_H \rangle.$$
 (66)

In the general case, the action of an XY-operator on the input phase $e^{ip_{\perp}^{\text{IN}}n_{\perp}}$ delivers a function of n_{\perp} , $\chi(n_{\perp})$, which depends on $\epsilon_1(n_{\perp})$, $\epsilon_2(n_{\perp})$ and p_{\perp}^{IN} . This function, $\chi(n_{\perp})$, contains the information from the propagation of the IN phase through the entire non-magnetic media, all the way to the OUT. Here, for Channel 3 SS,

Operator-XY₃^{SS}
$$(e^{ip_{\perp}^{\text{IN}}n_{\perp}}) = e^{ip_{\perp}^{\text{IN}}n_{\perp}}\chi_3^{S^{OUT},S^{IN}}(n_{\perp}).$$
 (67)

Henceforth, to keep the formulas for $\chi(n_{\perp})$ simple, we write interchangeably $p_x = p_x^{\rm IN}$ and $p_y = p_y^{\rm IN}$. However, to avoid confusion and to be able to distinguish between the IN and OUT phases, we will keep the index OUT for $p_{\perp}^{\rm OUT}$.

From (67) we deduce the dependence on $p_{\perp}^{\rm IN}$ of the χ -function. Namely, $\chi_3^{S^{OUT},S^{IN}}(n_{\perp}) = g_0 + g_1 \cos(ap_x) +$

 $g_2\cos(bp_y)+g_3\sin(ap_x)+g_4\sin(bp_y)+g_5\cos(ap_x-bp_y)+g_6\sin(ap_x-bp_y)$, where g_j , with $j=0\cdots 6$, are functions of n_\perp build exclusively on the non-magnetic materials deposited on the laminae. For example

$$g_{6} = \frac{i\epsilon_{1} (n_{x} - 1, n_{y} + 1) \epsilon_{2} (n_{x}, n_{y})}{a^{2}b^{2}\epsilon_{1} (n_{x}, n_{y} + 1)}$$

$$-\frac{i\epsilon_{1} (n_{x} + 1, n_{y} - 1) \epsilon_{2} (n_{x}, n_{y})}{a^{2}b^{2}\epsilon_{1} (n_{x} + 1, n_{y})}$$

$$+\frac{i\epsilon_{1} (n_{x} + 1, n_{y} - 1) \epsilon_{2} (n_{x} + 1, n_{y})}{a^{2}b^{2}\epsilon_{1} (n_{x} + 1, n_{y})}$$

$$-\frac{i\epsilon_{1} (n_{x} - 1, n_{y} + 1) \epsilon_{2} (n_{x}, n_{y} + 1)}{a^{2}b^{2}\epsilon_{1} (n_{x}, n_{y} + 1)}$$

$$+\frac{i\epsilon_{2} (n_{x}, n_{y} + 1)}{a^{2}b^{2}} - \frac{i\epsilon_{2} (n_{x} + 1, n_{y})}{a^{2}b^{2}},$$
(68)

where, for clarity, we used the shorthand notation $n_x-1=an_x-a,\ n_y+1=bn_y+b,$ and alike. The periodic boundary conditions and the sum from (65) bring in the Fourier transform of $\chi(n_\perp)$ over the variable $q_\perp=p_\perp^{\rm IN}-p_\perp^{\rm OUT}\equiv p_\perp-p_\perp^{\rm OUT},$

$$\tilde{\chi}_{3}^{S^{OUT},S^{IN}}(q_{\perp}) :=$$

$$(L_{x}L_{y})^{-1} \sum_{n_{\perp}} e^{iq_{\perp} \cdot n_{\perp}} \chi_{3}^{S^{OUT},S^{IN}}(n_{\perp}).$$
(69)

Since $\tilde{\chi}_3^{S^{OUT},S^{IN}}(q_{\perp})$ is common to all paths from Channel 3, the next focus is on the sum of all $\mathcal{Z}_{\text{paths}}$. It turns out that, for all channels, this sum factorizes into simple terms, each term being a function of either $\varphi_{z,\text{IN}}$ or $\varphi_{z,\text{OUT}}$, but not both. For the example under study

$$\sum_{\text{paths from Channel 3}} \mathcal{Z}_{\text{path}} = ic\Omega^2 \varphi_{z,\text{IN}} \varphi_{z,\text{OUT}}.$$
 (70)

Finally, we arrive at the contribution of Channel 3 $S^{OUT,+}, S^{IN,+}$, which, conveniently, is a product of $\tilde{\chi}_3$ from (69) and the channel \mathcal{Z} -factor (71)

$$\mathcal{Z}_{3}^{\text{OUT S+,IN S+}} = \|\text{OUT}\|^{-1} i c \Omega^{2} \varphi_{z,\text{IN}} \varphi_{z,\text{OUT}}.$$
 (71)

The main result, for the IN S to OUT S propagation, is that the transfer matrix element is reduced from a sum of 729 paths to a sum of 5 channels

$$T_{Sm,Sn}^{+,+} = \sum_{\text{channel}=1}^{5} \mathcal{Z}_{\text{channel}}^{\text{OUT S+,IN S+}} \, \tilde{\chi}_{\text{channel}}^{S^{OUT},S^{IN}}(q_{\perp}). \tag{72}$$

The dependence on the Bloch-Floquet indices m and n is through both p_{\perp} and q_{\perp} .

XII. Z AND XY-FACTORS FOR ALL CHANNELS

The XY-channel-operators for all four polarization combinations (OUT/IN,S/P) are represented in Fig.5. These operators are independent of the direction of propagation index \pm . The channels from IN S to OUT S were discussed above. There are 9 channels that connect IN S polarization with OUT P. All start with $|T_E\rangle$ and end in $\langle T_H|$. They are colored green in Fig.5. Change the input into a P-polarization. There are 5 unique channels that transfer an IN P into an OUT S. They are colored purple in Fig.5. The last case is the transfer of IN P into OUT P. There are 14 channels out of which 13 are unique to this polarization pair. They are colored black in Fig.5. The non-unique channel, shared with IN S to OUT S, has no (x,y)-dependence and so its χ -function is 1.

By contrast, the \mathbb{Z} -factors depend on the direction of propagation. Tab.III and Appendix B contain the information for all the other \mathbb{Z} -factors.

TABLE III. Unnormalized \mathcal{Z} factors for OUT S-, IN S-

(XY-operator) _{No.}	$\mathcal{Z}(\text{OUT }S-\ ,\ \text{IN }S-)\ \ \text{OUT}\ $
$(1)_1 \qquad \frac{i \langle p_{\perp}^{\text{OUT}} p_{\perp}^{\text{OUT}} \rangle ((\Omega^2 \varphi_z))}{c \varphi_{z, \zeta}^4}$	$\delta_{ ext{IN,OUT}} \delta_{ ext{IN,OUT}} \delta_{ ext{IN,OUT}}$
$(\langle T_H \epsilon_1 T_H \rangle)_2$	$-\frac{i\Omega^2\left(\Omega^2\varphi_{z,\mathrm{OUT}}+1\right)}{c\varphi_{z,\mathrm{IN}}\varphi_{z,\mathrm{OUT}}^2}$
$(\langle T_H \sigma_2 \epsilon_2 T_E \rangle \epsilon_1^{-1} \langle T_E \epsilon_1 \sigma_2 T_E)$	$(A)_3 - \frac{ic\Omega^2}{\varphi_{z,\text{IN}}\varphi_{z,\text{OUT}}}$
$(\langle T_H \epsilon_2 \epsilon_1 T_H \rangle)_4$	$\frac{i\Omega^4}{c\varphi_{z,\mathrm{IN}}\varphi_{z,\mathrm{OUT}}}$
$(\langle T_H \epsilon_2 T_H \rangle)_5$	$-\frac{i\Omega^2 \left(\Omega^2 \varphi_{z,\mathrm{IN}} + 1\right)}{c\varphi_{z,\mathrm{IN}}^2 \varphi_{z,\mathrm{OUT}}^2}$

^a The channel number is the No. index of XY-operator. Here $1-2\varphi_z+\Omega^2\varphi_z+\varphi_z^2=c^2\varphi_z \langle p_\perp|p_\perp\rangle$ and $\delta_{\rm IN,OUT}$ is the Kronecker delta.

The rule to obtain the \mathcal{Z} -factors for other directions is to change IN– into IN+ and, at the same time, change $\varphi_{z,\text{IN}} \to \varphi_{z,\text{IN}}^{-1}$ and $c \to -c$. The same rule applies for OUT– into OUT+.

However, this rule does not apply for Channel 1, for both SS and PP, Appendix B, Tables VII, IX. The reason is that, in vacuum, there are pairs of polarization and directions that cannot propagate into each other. For example, in vacuum, IN S+ cannot propagate into OUT S-. In contrast, Channel 1 is open in vacuum, so the rule does not apply to it.

At this point, the transfer matrix elements are computed in closed analytical formulas for any non-magnetic bilaminar lattice structure. The solution is completely general being valid for elaborate non-magnetic material patterns that can be drawn on both laminae.

The decomposition of propagation by channels can be implemented also for three or more patterned laminae. The number of channels increases with the increase of the number of laminae, but the procedure remains the

same.

Returning to the bilaminar structure, an avenue worth to explore is the continuum limit in the x and y dimensions. In this limit, the number of Bloch-Floquet modes become infinite, placing weight to our method of directly seizing the transfer matrix elements by circumventing infinite-dimensional transfer matrices.

XIII. CONTINUUM LIMIT FOR $a, b \rightarrow 0$

Consider that the discrete lattice constants a and b are much smaller than c, the discrete lattice constant on the z-axis. In this case n_{\perp} transforms into a continuum r_{\perp} coordinate so that the unit cell length is $l_x = \lim(aL_x)$ for $a \to 0$ and $L_x \to \infty$. Same goes for l_y . However, the z-axis remains discrete. In the continuum x,y-limit the discrete $\chi_3^{S^{OUT},S^{IN}}(n_{\perp})$, (67), is a function of (x,y)

$$\chi_{3}^{\text{InS,OutS}}(x, y, p_{x}, p_{y}) = p_{x} \left(i(\partial_{yy} \ln \epsilon_{1})(\partial_{x}\epsilon_{2}) - i(\partial_{xy} \ln \epsilon_{1})(\partial_{y}\epsilon_{2})\right) + p_{y} \left(i(\partial_{xx} \ln \epsilon_{1})(\partial_{y}\epsilon_{2}) - i(\partial_{xy} \ln \epsilon_{1})(\partial_{x}\epsilon_{2})\right) + p_{x}^{2}(\partial_{y} \ln \epsilon_{1})(\partial_{y}\epsilon_{2}) + p_{x}p_{y} \left(-(\partial_{x} \ln \epsilon_{1})(\partial_{y}\epsilon_{2}) - (\partial_{y} \ln \epsilon_{1})(\partial_{x}\epsilon_{2})\right) + p_{y}^{2} \left((\partial_{x} \ln \epsilon_{1})(\partial_{x}\epsilon_{2})\right).$$

$$(73)$$

The dependence of (73) on p_x , p_y is quadratic. Recall that $p_{\perp} = p_{\perp}^{\text{IN}}$. Each coefficient of this quadratic polynomial is a combination of partial derivatives of permittivities, Fig.6. We purposely placed these coefficients as a sum of terms, each being a product of a partial derivative of a function of ϵ_1 into another one, which depends exclusively on ϵ_2 . This specific arrangement is crucial to get a closed formula for the Fourier integral for a polygonal tessellated pattern, which will be a later subject to undertake. In addition to being technically useful, this arrangement has another facet. It reveals that the contribution of the permittivity constants to a channel is via pairs of functions (f_1, f_2) , where f_1 and f_2 acts only on ϵ_1 and ϵ_2 , respectively. From (73) we get $f_1(\epsilon_1) = \ln(\epsilon_1)$ and $f_2(\epsilon_2) = \epsilon_2$. These functions are easily gleaned, for each of the 33 channels, from Fig.6 and Appendix B. They are either $f(\epsilon) = \epsilon, \epsilon^{-1}, \ln(\epsilon)$ or the constant 1. All 33 channels, with the exception of the following 7 channels $\chi_{3,4}^{P^{OUT},S^{IN}}$, $\chi_4^{S^{OUT},P^{IN}}$, and $\chi_{7,8,9,13}^{P^{OUT},P^{IN}}$, use one pair (f_1,f_2) . Channel $\chi_8^{P^{OUT},P^{IN}}$ involves 3 pairs, whereas the other 6 from the exceptions use 2 pairs. Some examples are presented in Tab.IV. These channel-dependent permittivity functions are universal for a bilaminar structure, the distinction between devices with the same geometry being captured by the specific values of their arguments, ϵ_1 and ϵ_2 . It is worth noting that, for a given IN-OUT polarization pair, the

TABLE IV. Permittivity functions (f_1, f_2)

Channel	f_1, f_2
$\chi_3^{S^{OUT},S^{IN}}$	$f_1 = \ln(\epsilon), f_2 = \epsilon$
$\chi_2^{P^{OUT},S^{IN}}$	$f_1 = \epsilon, f_2 = \epsilon^{-1}$
$\chi_7^{P^{OUT},P^{IN}}$	$f_1 = \epsilon^{-1}, f_2 = 1 \text{ and } f_1 = \epsilon^{-1}, f_2 = \ln(\epsilon)$

^a Some channels, like χ_7 in this table, operates with more than one pair of permittivity functions.

set of functions are uniquely specific to a channel. This property can thus be used to name a channel. For example, Channel 3 in Fig.6 may bare the name $SS(\ln(x), x)$.

XIV. C-SCALING

The transfer matrix elements get simpler once the influence of the discreteness along the z-axis, c, is embodied into the scaling of the unit cell

$$x = cx', y = cy'. (74)$$

The frequency was already c-scaled in (34). All parameters become c-scaled $l_{x/y} = c l'_{x/y}$, $p_{x/y} = c^{-1} p'_{x/y}$. Scaling a χ channel-function is equivalent to multiplying it by a power of the scaling parameter c. For example, the c-scaling effect on (73) is

$$\chi_{3}^{\text{InS,OutS}}(x, y, p_x, p_y) = c^{-4} \chi_{3}^{\text{InS,OutS}}(x', y', p_x', p_y'). \tag{75}$$

In the continuum (x,y)-plane the discrete Fourier transform becomes an integral, as $(ab)/((aL_x)(bL_y)) \rightarrow (dx \ dy)/(l_x l_y)$. In the scaled variables, the Fourier transform of the χ channel-function

$$(l'_x l'_y)^{-1} \int_0^{l'_x} dx' \int_0^{l'_y} dy' e^{iq'_x x'} e^{iq'_y y'} \chi(x', y', p'_x, p'_y)$$
 (76)

is a function of $q_{\perp}^{'}=p_{\perp}^{'\mathrm{IN}}-p_{\perp}^{'\mathrm{OUT}}$ where $p_{x/y}^{'\mathrm{IN/OUT}}=2\pi\left(M_{x/y}^{\mathrm{IN/OUT}}+\xi_{x/y}\right)(l_{x/y}^{'})^{-1}$ with $2\pi\xi_{x}/l_{x}^{'}$ and $2\pi\xi_{y}/l_{y}^{'}$ being equal to $\Omega\sin(\theta)\cos(\phi)$ and $\Omega\sin(\theta)\sin(\phi)$, respectively.

For \mathcal{Z} -factors, the c-scaling appears in the argument of φ_z

$$\varphi_{z,\text{IN}} = \varphi_z \left(1 - 2^{-1}\Omega^2 + 2^{-1} \left(p_x^{'2} + p_y^{'2} \right) \right).$$
 (77)

For $\varphi_{z,\text{OUT}}$ the argument contains p'_{\perp}^{OUT} . Below, we drop the prime notation for the c-scaled parameters, understanding that all variables are c-scaled. The advantage of scaling is that the c-monomial from χ and its corresponding \mathcal{Z} -factor cancel, rendering a c-independent formula for a channel.

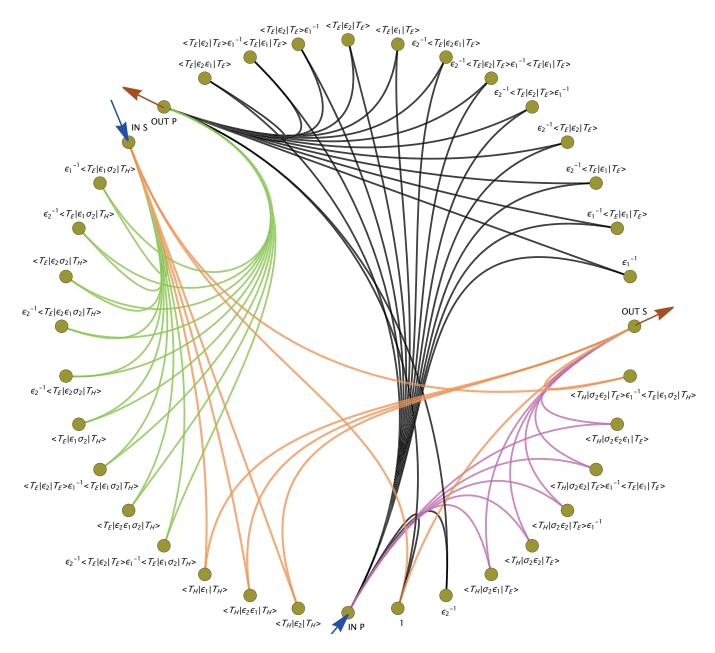


FIG. 5. There are 32 channels, ferreted out from 729 paths, that transfer the input fields into the output. Not all 32 channels are open for every polarization pairs. To use this figure, chose an input, either InS or InP. Then follow a line that connects the input with a disk, which represents a channel. From the disk, follow one of the lines that exit that disk and ends on a chosen output. The disks are labeled by the (x, y)-factor that defines the channel.

XV. POLYGONAL TESSELLATION PATTERNS

The transfer matrix elements, for the xy-continuous limit, are reduced at this point to the computation of 2-dimensional Fourier transforms of functions defined on the unit cell. To push forward the project of finding analytical closed-form formulas, we show that, in the general case, the Fourier transforms for all channels can be completely solved for polygonal subdomains. The approach and the notations for the general formulas are exemplified using a pattern, Fig.7, which we will call π - π -rig. The

unit cell is a square with corners positioned at $(\pm \pi, \pm \pi)$, in length units chosen for a desired frequency band. Inside the unit cell sits an inner square. Fig.7 shows two inner squares, one located on plane 1, whereas the other on plane 2, both defined in Fig.4. The corners of the unit cell are not visible in Fig.7 to save the space for the information pertaining to the inner squares. In the foreground, the square on plane 2 has its vertices labeled $B_{i,j}$, $i = \pm 1$, $j = \pm 1$ positioned at $(\pm \pi/2, \pm \pi/2)$. In the background, the square on plane 1, with vertices $A_{i,j}$, is rotated counterclockwise by an angle α . For $\alpha = 0$,

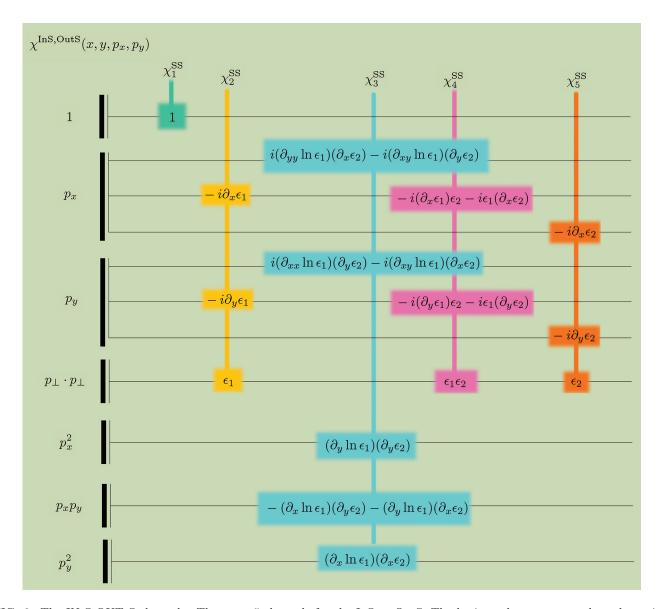


FIG. 6. The IN S OUT S channels. There are 5 channels for the InS to OutS. The horizontal staves carry the polynomials terms in p_x and p_y . The vertical structure of the figure shows the composition of each channel as a product of the polynomial term in p_x and p_y to its corresponding permittivity function. Recall that p_x and p_y denote the input values, although, for simplicity, they do not carry the index IN. The third column corresponds to formula (73). Appendix B contains the χ -functions for all the other polarization pairs.

the squares' vertices coincide. There are two kinds of points in Fig.7. Points like $A_{i,j}$ and $B_{i,j}$ from plane 1 and plane 2, respectively, are called real. In contrast, we call virtual those that appear as intersection points, like D_1 , the origin O and Δ_1 . All points, real and virtual, have associated with them a set of unit vectors. Take for example the origin O. There are four segments that originate at O. One is the segment $OA_{1,1}$ which carries a unit vector denoted $\hat{\mu}_1$ in Fig.7. Then $\hat{\mu}_2$, $\hat{\mu}_3$ and $\hat{\mu}_4$ are along $OB_{1,1}$, $OA_{-1,-1}$ and $OB_{-1,-1}$, respectively. All tails of these unit vectors sit on point O. From the same point O, originates another set of four unit vectors $\hat{\lambda}_i$, $i=1,\ldots,4$ in such a way that each pair $(\hat{\lambda}_i,\hat{\mu}_i)$ is orthogonal and

each triplet $(\hat{\lambda}_i, \hat{\mu}_i, \hat{z})$ is right-oriented. The last geometrical parameter is related to the choice of a frequency band, say in GHz or THz, which scales the device's units to mm or μ m, respectively. Versus this unit of length we define a unitless thickness parameter t

$$t = [1 \text{ unit}](c \text{ [unit]})^{-1}. \tag{78}$$

Although the frequency ω and the dimensions l_x, l_y are fixed in the chosen units, the c-scaled parameters change with t. As the laminae get thinner the scaled unit cell $(l_x^{'}, l_y^{'})$ and the probing wavelength $\lambda^{'}$ get larger, $\lambda^{'} = t \frac{\lambda^{'} [\text{unit}]}{1 [\text{unit}]}$, whereas the probing frequency Ω slides into lower regions, $\Omega = 2\pi \lambda^{'-1}$.

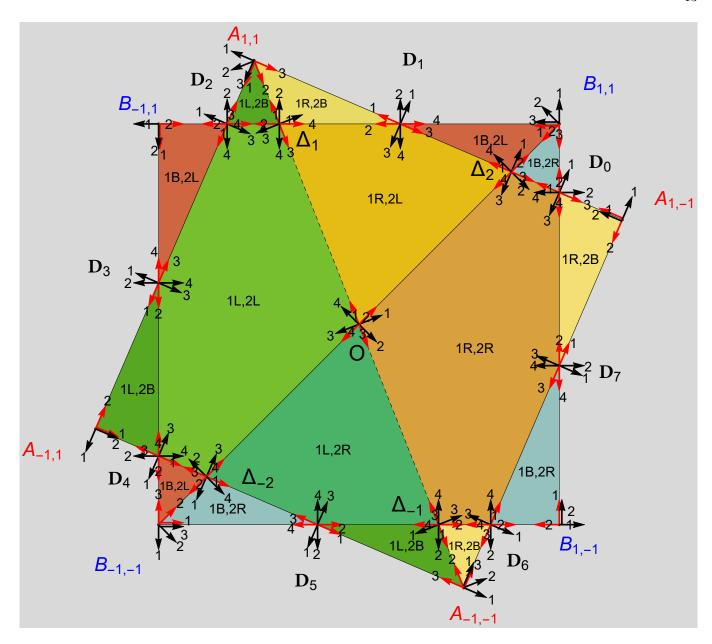


FIG. 7. The π - π -rig pattern. To relate to Fig.4, points denoted by A and B belong to plane 1 and 2, respectively. The \hat{z} -axis is coming out from the figure's page and \hat{x} is oriented from $B_{-1,-1}$ to $B_{1,-1}$. The real points, of V_1 and V_2 -type, are $A_{i,j}$ and $B_{i,j}$, $i=\pm 1, j=\pm 1$, respectively. The virtual points, V_{12} , at the intersection of one segment from lamina 1 and another from lamina 2, are D_m , $m=0,\cdots,7$, Δ_n , $n=\pm 1,\pm 2$ and the origin O. Here $\alpha>0$, so $A_{1,1}$ is rotated counterclockwise from its position on top of $B_{1,1}$ for $\alpha=0$. The black arrows represent the $\hat{\lambda}$ -vectors, whereas the red arrows represent the $\hat{\mu}$ -vectors. The permittivity ϵ_{1L} is printed on the left triangle $(A_{1,1},A_{-1,1},A_{-1,-1})$ whereas ϵ_{1R} on the right triangle $(A_{1,-1},A_{1,1},A_{-1,-1})$, both on lamina 1. Same goes for lamina 2 where ϵ_{2L} and ϵ_{2R} labels the left and right triangles with respect to the diagonal $B_{-1,-1}B_{1,1}$. Outside the interior squares, and up to the boundaries of the unit cell, the background permittivity ϵ_{1B} is printed on lamina 1 and ϵ_{2B} on lamina 2. The color and label of each polygon express the decomposition of the unit cell in polygons that carry a constant value of the product $\epsilon_1\epsilon_2$. The unit cell corners, which are not represented, own their own $(\hat{\lambda}, \hat{\mu})$ -pairs.

The increase of the scaled unit cell repositions the coordinates of the vertices, but do not change the unit vectors $(\hat{\lambda}, \hat{\mu})$.

The coordinates of all points, real and virtual, together with the orientations of all unit vectors and a choice of the thickness parameter comprise the geometrical data for computing the Fourier transformation of any polygonal tessellation. The other data come from the jumps of the permittivities across polygonal segments. For example, for point O in Fig.7 the relative permittivity pair $(\epsilon_{1R}, \epsilon_{2L})$ appears towards to tip of $\hat{\lambda}_1$, i.e. on the right-side looking along $\hat{\mu}_1$. The pair $(\epsilon_{1L}, \epsilon_{2L})$ sits towards

the tail of $\hat{\lambda}_1$, i.e. on the left-side of $\hat{\mu}_1$. As we cross $\hat{\mu}_1$ walking in the direction of $\hat{\lambda}_1$, slightly above point O, the change in the relative permittivities introduces a jump

$$(\Delta f_1 f_2)_{\mathcal{O}, \hat{\mu}_1} = f_1(\epsilon_{1R}) f_2(\epsilon_{2L}) - f_1(\epsilon_{1L}) f_2(\epsilon_{2L}), \quad (79)$$

where (f_1, f_2) is a channel-specific pair of permittivity functions as in Tab.IV.

The Fourier transforms for the χ channel-functions include both the geometrical configuration and the permittivities jumps. In (80) we show, as an example, the result of the Fourier transform, $\mathcal{F}(\chi)$, of the third channel for OutS,InS and for the specific case $q_{\perp} \cdot \hat{\mu} \neq 0$ for all $\hat{\mu}$,

$$\sum_{(V_{12},\hat{\mu})} e^{i(q_{\perp} \cdot V_{12})_2} (p_{\perp} \cdot \hat{\mu}_1) (p_{\perp} \cdot \hat{\mu}_2) \left(\frac{q_{\perp} \cdot \hat{\mu}_2}{\hat{\mu}_1 \cdot \hat{\lambda}_2}\right) \left(\frac{q_{\perp} \cdot \hat{\mu}_1}{\hat{\mu}_2 \cdot \hat{\lambda}_1}\right)
\Delta(\epsilon_2 \ln \epsilon_1)_{\hat{\mu}} \frac{W \cdot \hat{\lambda}}{W \cdot q_{\perp}} \frac{1}{q_{\perp} \cdot \hat{\mu}} -
\sum_{(V_{12},\hat{\mu})} e^{i(q_{\perp} \cdot V_{12})_3} (p_{\perp} \cdot \hat{\mu}_1) (\hat{\mu}_1 \cdot \hat{\lambda}_2) \left(\frac{q_{\perp} \cdot \hat{\mu}_2}{\hat{\mu}_1 \cdot \hat{\lambda}_2}\right)^2 \left(\frac{q_{\perp} \cdot \hat{\mu}_1}{\hat{\mu}_2 \cdot \hat{\lambda}_1}\right)
\Delta(\epsilon_2 \ln \epsilon_1)_{\hat{\mu}} \frac{W \cdot \hat{\lambda}}{W \cdot q_{\perp}} \frac{1}{q_{\perp} \cdot \hat{\mu}}.$$
(80)

For each virtual vertex V_{12} from Fig.7, the sum covers all four $\hat{\mu}'$ s associated with it. The indices 1 and 2 refer to the line from plane 1 and 2, respectively. In this formula we are free to choose one pair $(\hat{\mu}_1, \hat{\mu}_2)$ of unit vectors along line 1 and line 2, out of all four possible choices of the pairs exiting V_{12} . The result is independent on the choice of the pair because the terms are invariant to the transformation $\hat{\mu}_1 \to -\hat{\mu}_1$ or $\hat{\mu}_2 \to -\hat{\mu}_2$.

The Fourier transform in (80) depends on p_{\perp} , i.e. $p_{\perp}^{\rm IN}$, because the channel's χ -function (73) depends on it. In addition, the transform is naturally a function of the q_{\perp} , (76). The first sum in (80) displays the quadratic dependence on p_{\perp} as a dot product, invariant to rotations of the (x,y) coordinate system. An invariant form also appears for the second sum, which contains the linear dependence on p_{\perp} . In this formula, the variables q_{\perp}, p_{\perp} and V_{12} are c-scaled and depend on the thickness parameter t. As we announced before, we do not carry the primed symbol, (74), anymore. In the next section we lay down the Fourier transform results, with their proofs left to Appendices D to H.

XVI. FOURIER TRANSFORMS FOR THE χ – channel-functions

We encounter four types of integrals on the unit cell, based on the number of derivatives $m^1 = (m_x^1, m_y^1)$ and $m^2 = (m_x^2, m_y^2)$ being zero or not

(00).
$$\iint dx dy(f_1)(f_2)e^{q_{\perp} \cdot r_{\perp}}, m^1 = 0, m^2 = 0,$$

(10).
$$\iint dx dy (\partial_{m^1} f_1)(f_2) e^{q_{\perp} \cdot r_{\perp}}, \ m^1 \neq 0, m^2 = 0,$$

(01).
$$\iint dx dy(f_1)(\partial_{m^2} f_2)e^{q_{\perp} \cdot r_{\perp}}, \ m^1 = 0, m^2 \neq 0,$$

(11).
$$\iint dx dy (\partial_{m^1} f_1)(\partial_{m^2} f_2) e^{q_{\perp} \cdot r_{\perp}}, \ m^1 \neq 0, m^2 \neq 0.$$

There are three cases for (00), which depend on the relation between the geometry of the device, expressed by the set of vectors $\hat{\mu}$ and the mode-scattering vector q_{\perp} . For case (1), $q_{\perp} \cdot \hat{\mu} \neq 0$. Case (2) consists of $q_{\perp} \cdot \hat{\mu} = 0$ and $q_{\perp} \neq 0$, which means that $q_{\perp} = \pm \hat{\lambda} |q_{\perp}|$. Finally for (3) $q_{\perp} = 0$.

The formulas for (00), from (81) and (82), are written on purpose as a sum of terms contributed by each pair $(V, \hat{\mu})$. This is akin to a potential theory where only the ends of the curve contribute. In addition, also reminiscent of a potential theory, gauge vectors appear in the solution. They are the same for all pairs $(V, \hat{\mu})$ and their arbitrariness helps eliminating all singularities that may appear in the denominators. The gauge vectors are denoted as W and \mathcal{D} , and can be arbitrarily chosen with the provision that $W \cdot q_{\perp} \neq 0$ and $\mathcal{D} \cdot \hat{\mu} \neq 0$. The jump in ϵ , as the vector $\hat{\mu}$ is traversed along $\hat{\lambda}$, is captured in $(\Delta f_1 f_2)_{\hat{\mu}}$, as exemplified in (79).

Outside the unit cell we place a fictitious material with $\epsilon = 0$ to get, for the (00) integrals, the correct terms generated by the unit cell boundaries.

The (00) integration formula for a polygonal tessellation of the unit cell, for cases (1) and (2), is

$$\iint dx dy (f_1 f_2) e^{iq_{\perp} \cdot r_{\perp}} =$$

$$\sum_{V,\hat{\mu}} e^{iq_{\perp} \cdot V} \frac{1}{q_{\perp} \cdot \hat{\mu}} \frac{W \cdot \hat{\lambda}}{W \cdot q_{\perp}} (-\Delta(f_1 f_2))_{\hat{\mu}} +$$

$$\sum_{V,\hat{\mu}} e^{iq_{\perp} \cdot V} (i\hat{\mu} \cdot V) \frac{W \cdot \hat{\lambda}}{W \cdot q_{\perp}} (-\Delta(f_1 f_2))_{\hat{\mu}} .$$
(81)

The first and the second sum applies for case(1) and (2), respectively. For (00) in case (3) we need to use two gauge vectors. The W is the same as before, whereas \mathcal{D} is specific for this case and comes from taking the limit $s \to 0$ for $q_{\perp} = s\mathcal{D}$. This formula,as proven in Appendix E, is independent on the choice of \mathcal{D}

$$\iint dx dy (f_1 f_2) =$$

$$\sum_{V,\hat{\mu}} \frac{1}{2} (i\mathcal{D} \cdot V)^2 \frac{1}{\mathcal{D} \cdot \hat{\mu}} \frac{W \cdot \hat{\lambda}}{W \cdot \mathcal{D}} (-\Delta(f_1 f_2))_{\hat{\mu}} .$$
(82)

We intentionally drafted the (00) Fourier transforms as a sum of contributions from vertices. This format can be handed on to the next integrals, (01), (1,0) and (1,1), in a consistent manner. The (00) integral appear in other works [35],[36], but as a sum over the edges of the polygon.

For the formulas that follow, we will list only the contribution of a pair $(V, \hat{\mu})$, the summation being understood.

XVII. FOURIER TRANSFORMS FOR PRODUCT OF DERIVATIVES OF TYPE (01), (10) AND (11)

The result for the (00) case is now used to generate the integrals for which a derivative acts on at least one function. The procedure implies two steps. The first step is to compute

$$\iint dx dy f_1(r_{\perp} + \delta r_1) f_2(r_{\perp} + \delta r_2) e^{iq_{\perp} \cdot r_{\perp}} =$$

$$\operatorname{Int}(\delta x_1, \delta y_1, \delta x_2, \delta y_2)$$
(83)

as a function of two independent translations, δr_1 and δr_2 , on plane 1 and plane 2, respectively. These translations change the position of a vertex V

$$V_{\text{translated}} = V - \overrightarrow{\tau}_x^1 \delta x_1 - \overrightarrow{\tau}_y^1 \delta y_1 - \overrightarrow{\tau}_x^2 \delta x_2 - \overrightarrow{\tau}_y^2 \delta y_2. \tag{84}$$

The four vectors $\vec{\tau}$ depend on the vertex V being subjected to a free or constraint translation, which will be defined subsequently. If the vertex is associated with a free translation, we have $\vec{\tau}_x^1 = \vec{\tau}_x^2 = \hat{x}$ and $\vec{\tau}_y^1 = \vec{\tau}_y^2 = \hat{y}$. A vertex at the intersection of two lines from different planes, subjected to a constraint translation, moves to

$$(V_{12})_{\text{translated}} = V_{12} - \frac{\delta r_1 \cdot \hat{\lambda}_1}{\hat{\mu}_2 \cdot \hat{\lambda}_1} \hat{\mu}_2 - \frac{\delta r_2 \cdot \hat{\lambda}_2}{\hat{\mu}_1 \cdot \hat{\lambda}_2} \hat{\mu}_1, \quad (85)$$

where $\hat{\mu}_1$ and $\hat{\mu}_2$ represent the directions of the two intersecting lines situated on plane 1 and 2, respectively. For constraint translations, the vectors $\vec{\tau}^1$ and $\vec{\tau}^2$ can be extracted from (85). In what follows we associate vertices V_1 and V_2 that are exclusively situated either in plane 1 or 2, respectively, to a free translation. For a V_1 -type vertex $\vec{\tau}^2 = 0$ and, in reverse, $\vec{\tau}^1 = 0$ for a V_2 -type. Virtual vertices V_{12} are associated to a constraint translation. The sets V_1 , V_2 and V_{12} are exemplified in Fig.7.

For the second step, once the function $\operatorname{Int}(\delta x_1, \delta y_1, \delta x_2, \delta y_2)$ is at hand, we compute the rest of the integrals by taking its derivatives

$$\iint dx dy \left(\partial_x^{m_x^1} \partial_y^{m_y^1} f_1(r_\perp)\right) \left(\partial_x^{m_x^2} \partial_y^{m_y^2} f_2(r_\perp)\right) e^{iq_\perp \cdot r_\perp}$$

$$= \partial_{\delta x_1}^{m_x^1} \partial_{\delta y_1}^{m_y^1} \partial_{\delta x_2}^{m_x^2} \partial_{\delta y_2}^{m_y^2} \text{Int}$$
(86)

at δx_j , $\delta y_j = 0$, j = 1, 2. The results are listed below and the details follow in Appendices D to H.

Unlike for the (00) integrals, here the unit cell boundaries do not generate any terms, because the derivative of a permittivity function is zero across the unit cell boundaries

For $m^1 + m^2 \neq 0$ and case (1), $q_{\perp} \cdot \hat{\mu} \neq 0$, the contri-

bution of $(V, \hat{\mu})$ is

$$e^{i(q_{\perp}\cdot V)} \left(-iq_{\perp}\cdot \overrightarrow{\tau}_{x}^{1}\right)^{m_{x}^{1}} \left(-iq_{\perp}\cdot \overrightarrow{\tau}_{y}^{1}\right)^{m_{y}^{1}}$$

$$\left(-iq_{\perp}\cdot \overrightarrow{\tau}_{x}^{2}\right)^{m_{x}^{2}} \left(-iq_{\perp}\cdot \overrightarrow{\tau}_{y}^{2}\right)^{m_{y}^{2}}$$

$$\frac{1}{q_{\perp}\cdot \hat{\mu}} \frac{W\cdot \hat{\lambda}}{W\cdot q_{\perp}} \left(-\Delta(f_{1}f_{2})_{\hat{\mu}}\right).$$

$$(87)$$

For case (2), $q_{\perp} \cdot \hat{\mu} = 0$, the contribution of $(V, \hat{\mu})$ is

$$\frac{d}{ds}\Big|_{s=0} e^{i(q_{\perp} + s\hat{\mu}) \cdot V} \left(-i(q_{\perp} + s\hat{\mu}) \cdot \vec{\tau}_{x}^{1} \right)^{m_{x}^{1}}$$

$$\left(-i(q_{\perp} + s\hat{\mu}) \cdot \vec{\tau}_{y}^{1} \right)^{m_{y}^{1}} \left(-i(q_{\perp} + s\hat{\mu}) \cdot \vec{\tau}_{x}^{2} \right)^{m_{x}^{2}}$$

$$\left(-i(q_{\perp} + s\hat{\mu}) \cdot \vec{\tau}_{y}^{2} \right)^{m_{y}^{2}} \frac{W \cdot \hat{\lambda}}{W \cdot q_{\perp}} \left(-\Delta (f_{1}f_{2})_{\hat{\mu}} \right).$$
(88)

For case (3), $q_{\perp} = 0$, the contribution of $(V, \hat{\mu})$ is

$$\frac{1}{2} \frac{d^{2}}{ds^{2}} \Big|_{s=0} e^{i(s\mathcal{D}\cdot V)} s^{m_{x}^{1} + m_{y}^{1} + m_{x}^{2} + m_{2}^{2}}$$

$$(-i\mathcal{D} \cdot \vec{\tau}_{x}^{1})^{m_{x}^{1}} (-i\mathcal{D} \cdot \vec{\tau}_{y}^{1})^{m_{y}^{1}} (-i\mathcal{D} \cdot \vec{\tau}_{x}^{2})^{m_{x}^{2}}$$

$$(-i\mathcal{D} \cdot \vec{\tau}_{y}^{2})^{m_{y}^{2}} \frac{W \cdot \hat{\lambda}}{W \cdot \mathcal{D}} (-\Delta (f_{1}f_{2})_{\hat{\mu}}).$$
(89)

The transfer matrix for a polygonal tessellated bilaminar non-magnetic structure, continuous in the x and y directions, is completely solved at this point. We are moving to test the theoretical results by comparing our closed analytical formulas for the π - π -rig structure, to numerical results obtained from a high-performance analysis software package [37]. Complex symbolic computations were handled by [38].

XVIII. EVANESCENT RESONANT MODES BY OPTIMIZATION DESIGN

The intent is to design-optimize a dielectric structure from Fig.7 such that a subset of evanescent Bloch-Floquet modes $(M_x, M_y) \neq 0$ acquire large scattering matrix elements at a specified frequency. Such an excited resonant mode propagates along the plane (x, y) at a frequency smaller than its Rayleigh frequency. Specifically, in the frequency range under study, 37 GHz to 50 GHz, the optimization function is based on four modes. Two modes, (0,0) and (-1,0), propagate, and two other modes, $(0,\pm 1)$, are evanescent. The goal is to find a set of dielectric constants for which the modes $(0,\pm 1)$ resonate. To excite the resonant modes, the plane wave (0,0) coming from z-min lands at angles $\theta = 17.5^{\circ}$ and $\varphi = 0^{\circ}$ on the face A of the π - π -rig oriented at $\alpha = 45^{\circ}$. The thickness of each of the two laminae is $c = 0.25 \, \mathrm{mm}$. The design-objective-function, constructed from the analytical formulas for the transfer matrix elements, selects a point in the 6-dimensional dielectric space $\epsilon_{1B} = 4.99$, $\epsilon_{2B} = 2.96, \; \epsilon_{1L} = 7.60, \; \epsilon_{2L} = 5.66, \; \epsilon_{1R} = 5.93 \; \text{and}$ $\epsilon_{2R} = 1.63.$

Technologically, this point may not be easily implemented, although we constrained the dielectric constants to be less than 12. Instead, we focus on studying the predictions put forward by the analytic solution and compare them against numerical results from a high-performance software package.

These predictions are grouped in three categories. The first category, inspired by topological photonics, is related to robustness of the resonant modes with respect to the change of the dielectric constants, quantified as a map from the real to integer numbers. The second is based on resonant frequency identification, whereas the third is focused on high Q-factors and the use of complex frequency plane to estimate the Fano-Lorentz spectral line shape for the resonant modes. In what follows we confine ourselves to evanescent S-polarized resonant waves excited by the (0,0) S-polarized incoming wave. Only the main results are presented below, with specific details on the design optimization being summarized in Appendix I.

XIX. A MAP FROM THE REAL TO INTEGER NUMBERS

The resonances in the scattering matrix elements appear as zeros of the determinant of the $T^{-,-}$ matrix, (51). The minimal $T^{-,-}$ matrix can be reduced to just the matrix element $T_{Sm,Sm}^{-,-}$, the zeros of which give the first approximation for the resonant frequencies. To see that, take a 2×2 transfer matrix built only from the set $T_{Sm,Sm}^{\pm,\pm}$ and look at the resonance for the mode Sm as a singularity for which (49) has a non-zero solution if all coefficients but (DIR,POL,BF)=(+,S,m) and (dir,pol,bf)=(-,S,m)are zero. It turns out that this simple approximation has predictive power. As the dielectric constants change their values, the zeroes of $T_{Sm,Sm}^{-,-}$ appear or disappear, creating or destroying a resonance. We study this phenomenon for variable $\epsilon_{1B} = \epsilon_{2B}$, running from 1 to ∞ , with the rest of the dielectric constants kept constant at the optimized values.

Hence, map $\epsilon_{1B} = \epsilon_{1B}$ to the number of modes $m = (M_x, M_y)$ for which the diagonal transfer matrix element $T_{Sm,Sm}^{-,-}$, Appendix C, has at least one zero on the frequency axis in the interval [0, 60] GHz,

$$\epsilon \in \mathbb{R} \mapsto \text{number of modes with zeroes.}$$
 (90)

The analytic formulas position the zeros as in Fig.(8) and Fig.(9)

As $\epsilon_{1\mathrm{B}} = \epsilon_{2\mathrm{B}}$ increases from 1 to ∞ , Fig.10, the number of modes for which $T_{Sm,Sm}^{-,-}$ crosses the real frequency axis increases in discontinuous steps, then decreases as the dielectric constant gets above 30. It reaches a plateau of 36 modes as $\epsilon \to \infty$. Fig.11 shows the position in the (M_x, M_y) plane of the 53 and 36 modes for $\epsilon_{1\mathrm{B}} = \epsilon_{2\mathrm{B}} = 35$ and ∞ , respectively. Two adjacent steps in Fig.10 have two distinct topological invariants,

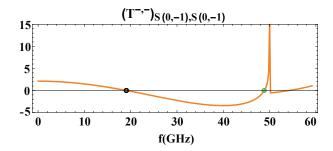


FIG. 8. The theoretical matrix element $T_{S(0,-1),(S(0,-1))}^{-,-}$ as a function of frequency. The zeroes at 19.9 GHz and 48.86 GHz have a negative and a positive slope, respectively. The Rayleigh frequency for the mode (0,-1) is at 50.03 GHz, where a pole singularity is present. The dielectric constants are $\epsilon_{1\mathrm{B}}=\epsilon_{2\mathrm{B}}=35$.

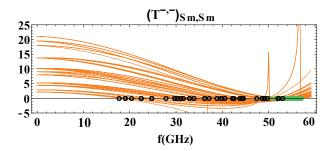


FIG. 9. All matrix elements $T_{Sm,Sm}^{-,-}$ that have at least one zero on the real frequency axis. The zeroes with a negative slope are marked as empty black circles, whereas the zeroes with a positive slope are in green. There are three pole singularities in the range of frequency up to 60 GHz, for $(-1,0),(0,\pm1)$ and $(-1,\pm1)$ at 36.69,50.03 and 56.71 GHz, respectively.

i.e. distinct number of resonant modes. The boundaries of these steps are not uniformly distributed on the horizontal dielectric axis. Knowing the distribution of these boundary values may play a significant role in assembling compound devices, which are built by bringing together two structures with distinct topological invariants. Numerical simulations confirm that 5 modes resonate for $\epsilon_{1B} = \epsilon_{2B} = 1$ and 53 for $\epsilon_{1B} = \epsilon_{2B} = 35$.

One step deeper into the analysis of the zeros is provided by propagation along channels. Channel 1 SS does not depend on the dielectric constants and is positive for any frequency and direction p_{\perp} , Fig.12. Some other channels have to be negative for $T_{Sm,Sm}^{-,-}$ to cross the frequency axis. Interestingly, each channel keeps a constant sign as a function of frequency, namely (1,+), (2,-), (3,-), (4,+) and (5,-), noticeable in Fig.13 to Fig.16.

From Fig.14 we see that Channel 3 is two orders of magnitude smaller than the other ones, so it does not lead to creation of destruction of a zero, but contributes to its location on the frequency axis. As $\epsilon_{1B} = \epsilon_{2B}$ increases the

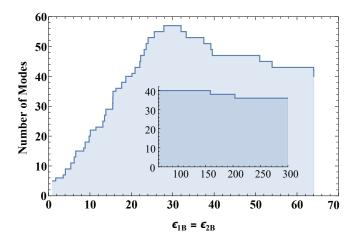


FIG. 10. The topological map of the number of modes $m = (M_x, M_y)$ for which the corresponding diagonal transfer matrix element $T_{Sm,Sm}^{--}$ has a zero on the real frequency axis in the interval [0,60] GHz. The continuous variable $\epsilon_{1B} = \epsilon_{2B}$ runs from 1 to ∞ .

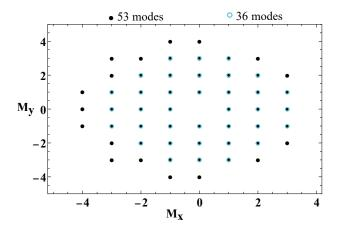


FIG. 11. Modes $m=(M_x,M_y)$. There are 53 modes for $\epsilon_{1\mathrm{B}}=\epsilon_{2\mathrm{B}}=35$ and 36 modes for ∞ , respectively.

negative contribution starts to dominate the positive one and two phenomena appear: the zeros are pushed into lower frequencies and a variable number of modes start to cross the frequency axis. This explains the increase in the number of resonant modes as $\epsilon_{1B} = \epsilon_{2B}$ increases.

A. Zeroes of the diagonal matrix elements of $T^{-,-}$

A distinctive advantage of analytical formulas over the numerical approaches is in the study of infinite limits

$$\epsilon_{1B} = \epsilon_{2B} \to \infty.$$
(91)

In this limit, the zeros of the transfer matrix elements $T_{Sm,Sm}^{-,-}(\Omega) = 0$, appear at small $\Omega \cong 0$. So, approximate

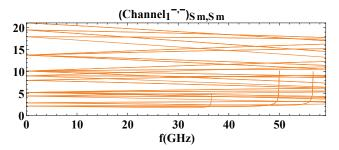


FIG. 12. Channel 1 for all 53 matrix elements $T_{Sm,Sm}^{-,-}$ from Fig.11. Channel 1 is independent on ϵ .

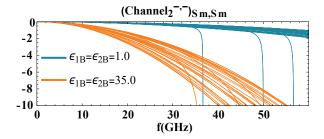


FIG. 13. Channel 2 for all 53 matrix elements $T_{Sm,Sm}^{-,-}$ from Fig.11, for two values of $\epsilon_{1\mathrm{B}}=\epsilon_{2\mathrm{B}}$.

 $1 + \Omega^2 \varphi_{z,\text{OUT}} \cong 1$ to get, from Appendix C,

$$(T_{Sm,Sm}^{-,-})_{\text{Channel 1}} \cong \frac{1}{\varphi_{z,\text{OUT}}^3},$$
 (92)

$$(T_{Sm,Sm}^{-,-})_{\text{Channel 2}} \cong -\frac{\Omega^2}{8\varphi_{z,\text{OUT}}^2 \left(1-\varphi_{z,\text{OUT}}^2\right)} \left(6\epsilon_{1\text{B}}\right),$$

$$(T_{Sm,Sm}^{-,-})_{\text{Channel }3} \cong 0,$$

$$(T_{Sm,Sm}^{-,-})_{\mathrm{Channel}\ 4} \cong \frac{\Omega^4}{\varphi_{z,\mathrm{OUT}} \left(1 - \varphi_{z,\mathrm{OUT}}^2\right)} \left(\frac{\epsilon_{1\mathrm{B}}\epsilon_{2\mathrm{B}}}{\sqrt{2}}\right),$$

$$(T_{Sm,Sm}^{-,-})_{\text{Channel 5}} \cong -\frac{\Omega^2}{8\varphi_{z,\text{OUT}}^2 \left(1-\varphi_{z,\text{OUT}}^2\right)} \left(6\epsilon_{2\text{B}}\right).$$

The equation $(T_{Sm,Sm}^{-,-})=0$, under the above approximations and using the notation $\epsilon_{1\mathrm{B}}=\epsilon_{2\mathrm{B}}=\epsilon$, turns into

$$-\frac{3}{2}\Omega^2 \varphi_{z,\text{OUT}} \epsilon + \frac{1}{\sqrt{2}}\Omega^4 \varphi_{z,\text{OUT}}^2 \epsilon^2 + 1 - \varphi_{z,\text{OUT}}^2 = 0. \tag{93}$$

As $\epsilon \to \infty$, the zero of $T_{Sm,Sm}^{-,-}(\Omega) = 0$ tends to zero in such a way that $\Omega^2 \epsilon \to$ finite number. In terms of this finite number, which we call X, the equation becomes

$$-\frac{3}{2}X\varphi_{z,\text{OUT}} + \frac{1}{\sqrt{2}}X^2\varphi_{z,\text{OUT}}^2 + 1 - \varphi_{z,\text{OUT}}^2 = 0. \quad (94)$$

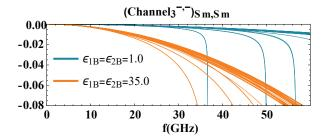


FIG. 14. Channel 3 for all 53 matrix elements $T_{Sm,Sm}^{-,-}$ from Fig.11, for two values of $\epsilon_{1\mathrm{B}}=\epsilon_{2\mathrm{B}}$.

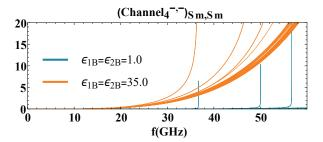


FIG. 15. Channel 4 for all 53 matrix elements $T_{Sm,Sm}^{-,-}$ from Fig.11, for two values of $\epsilon_{1\mathrm{B}} = \epsilon_{2\mathrm{B}}$.

The requirement for X to be positive imposes a constrain on mode numbers M_x and M_y , for which the diagonal transfer matrix elements posses a zero on the real frequency axis, in the limit $\epsilon_{1\mathrm{B}} = \epsilon_{2\mathrm{B}} \to \infty$

$$\varphi_z \left(\frac{1}{2} \left(\frac{M_x^2}{t^2} + \frac{M_y^2}{t^2} \right) + 1 \right) \geqslant \frac{1}{4} \sqrt{16 - 9\sqrt{2}}.$$
(95)

This inequality is valid for 36 modes, which are visible in Fig.11.

XX. ANALYTICAL PREDICTION OF THE RESONANT FREQUENCY

A. Thinner the lamina higher the precision

From counting the number of zeros for many modes, we change the focus, TableV, to predict the position of the zero, Ω_{theory} , of $T_{Sm,Sm}^{-,-}$ for the optimized design modes, $(0,\pm 1)$. Both modes have the same zero at $\varphi=0^{\circ}$. The resonant frequency depends on the thickness of the structure's lamina, c. All the other parameters are kept constant.

Notice that Ω %-error = $100\frac{|\Omega \text{ num} - \Omega \text{ theory}|}{\Omega \text{ num}}$, which measures the distance to the numerical simulation result $\Omega \text{ num}$, [37], decreases with the decrease of the width c. This is to be expected because as $c \to 0$ the discrete approximation of Maxwell's equations improves.

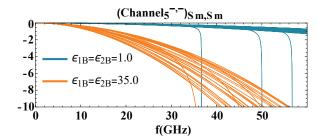


FIG. 16. Channel 5 for all 53 matrix elements $T_{Sm,Sm}^{-,-}$ from Fig.11, for two values of $\epsilon_{1B} = \epsilon_{2B}$.

TABLE V. Variable layer width.

c [mm]	t	f[GHz]	Ω num	$\Omega\mathtt{theory}$	$\Omega\%-{\tt error}$
0.100	10	47.540	0.0996365	0.0993646	0.27
0.200	5	43.376	0.181819	0.180396	0.78
0.250			0.218319	0.215294	1.39
0.275	4/11	40.693	0.234537	0.231701	1.21
0.300	10/3	39.908	0.250923	0.247551	1.34

B. The influence of the rotation angle α on the resonant frequency

Out of the 5 channels for transfer of the SS-polarization, only Channels 3 and 4 depend on the angle α . As the angle α is varied, the resonant frequency for the degenerate modes (0,-1) and (0,1) changes in the vicinity of the frequencies determined at $\alpha=45^{\circ}$, Figs.17,18. Although the relative changes are small, with an estimated linear slope of $-0.96 \mathrm{MHz/deg}$ and $-2.46 \mathrm{MHz/deg}$, respectively, the slopes are close to the ones from the numerically simulated data. The system-

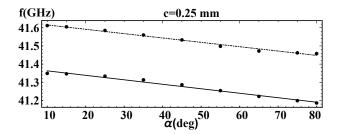


FIG. 17. The resonant frequency of the modes S(0,-1) and S(0,1) as a function of α . The dotted-dashed line corresponds to the numerical data, whereas the continuum line to the analytical transfer matrix.

atic shift between the theoretical and numerical values, described for $\alpha=45^\circ$ in Tab.V, is the same for all angles α .

The study of the wedge effect, that comes out for $0^{\circ} < \alpha < 10^{\circ}$ or for $80^{\circ} < \alpha < 90^{\circ}$, will be covered in a different manuscript.

The transfer matrix elements depend on the logarithm of the permittivities, so we need to test the formulas for

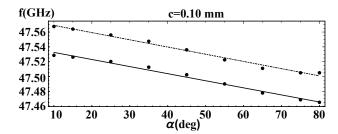


FIG. 18. The resonant frequency of the modes S(0,-1) and S(0,1) as a function of α . The dotted-dashed line corresponds to the numerical data, whereas the continuum line to the analytical transfer matrix.

a metal, which exhibits complex permitivitty. We take $\epsilon_{2\mathrm{B}} = \mathrm{Johnson}$ -Chrysti gold and find a local minimum of an objective function in the 5-dimensional space of the other dielectric constants. The frequency range is now placed in the infrared at f = 286.2 THz. The optimization process to find the five unknown dielectric constants is similar to that for the all-dielectric case. This time, though, the objective function is based on one propagative mode (0,0) and one evanescent mode (-1,0), both P-polarized. The position and shape of the theoretical resonance were confirmed by numerical simulations performed via [37].

XXI. A HIGH Q-FACTOR BILAMINAR STRUCTURE

To study the theoretical prediction for the amplitude we choose a series of resonances with large Q-factors. The first has $Q=4.8\times 10^6$ at -3 dB, Fig.19. The theoretical values were computed using a 20×20 transfer matrix. Two systematic shifts, $f_{\rm shift}$ and $t_{\rm shift}$, are needed to superpose the theoretical formula $20\log_{10}\left|t_{S(0,1),S(0,0)}^{max,min}(f-f_{\rm shift})\right|+t_{\rm shift}$ on numerical simulations. For Fig.19, $f_{\rm shift}=3.2\ 10^{-5}$ GHz and $t_{\rm shift}=-3.9$ dB. The lamina being thin, c=0.01mm, the shifts are small with respect to the frequency and amplitude at resonance.

Variable φ offers another venue to study the amplitude around a high Q-factor resonance. The modes (0,-1) and (0,1) are degenerate for $\varphi=0^\circ$, having the same Rayleigh and resonant frequency. As the angle φ slides away from 0° , the scattering amplitude of the mode S(0,-1) decreases, whereas the scattering amplitude for the mode S(0,1) remains excited at high dB levels, Fig.20. The same trend was confirmed by numerical simulation. TableVI contains additional data for the comparison between theory and numerical simulations for the high Q-factors.

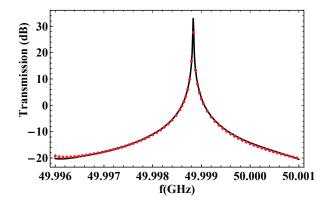


FIG. 19. A resonance with a high Q-factor. The Q-factor at -3 dB is $Q=4.8\times 10^6$. The black curve represents the theoretical transmission from S(0,0) at z-min to S(0,1) at z-max. The red points were numerically simulated via [37]. All parameters are equal to the optimized values except for $c=0.01 \mathrm{mm}$ and $\epsilon_{2\mathrm{R}}=1.0$.

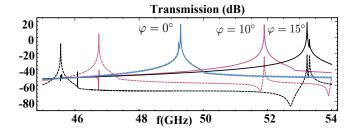


FIG. 20. Resonances with a high Q-factor for variable incident angle φ . The parameters are c=0.05 mm and $\varphi=0^{\circ},10^{\circ},$ and 15° . All the other parameters are placed at the optimized values. The continuous and dashed curves represent the theoretical transmission from S(0,0) at z-min to S(0,1) and S(0,-1) at z-max, respectively. For $\varphi=0^{\circ},10^{\circ}$ and $\varphi=15^{\circ}$, the resonant frequency, in GHz, and the Q-factors are $(49.30,3.6\times10^4),(51.90,5.2\,10^3)$ and $(53.24,1.3\,10^4)$, respectively.

XXII. COMPLEX-FREQUENCY PLANE AND THE WEIGHTED FANO-LORENTZ LINE SHAPE

Moving beyond predicting the position of the resonant frequency and its amplitude, the complete analytical solution for transfer matrix provides a simple but meaningful approximation for the resonant line shape

$$t_{S(0,1),S(0,0)}^{min,max} = \frac{\text{Cofactor}_{S(0,0),S(0,1)}(T^{-,-})}{\text{Det}(T^{-,-})}$$
$$\cong \rho e^{i\Phi} \frac{f - f_{zero}}{f - f_{pole}}, \tag{96}$$

where the zero and the pole are located in the complex frequency plane, both in the vicinity of the real resonant frequency, [33]. The meromorphic approximation (96) has a natural structure of dipoles with the monopoles placed at f_{zero} and f_{pole} , Fig.21.

TABLE VI. Variable c for $\varphi=15^{\circ}$. Scattering matrix element for input S(0,0) at z-min output S(0,1) at z-max. Frequency shifts are measured in GHz and the amplitude of shifts of the Scattering matrix elements in dB.

c[mm]	$ m f_{shift}$	$t_{ m shift}$	Q
0.25	$3.2 \ 10^{-1}$	9.81	$1.1 \ 10^3$
$0.10 \\ 0.05$	$5.4 \ 10^{-2}$ $9.4 \ 10^{-3}$	$5.67 \\ 2.85$	$2.6 \ 10^3$ $1.3 \ 10^4$
0.01	$9.0 \ 10^{-5}$	-3.78	$1.2 10^6$

To estimate the pole and the zero, we use $\varphi_z(\zeta)$ already defined for complex values of ζ . Here we take advantage of the continuity at the real ζ -axis of $\varphi_z(\zeta)$ coming from below, $\operatorname{Im}(\zeta) \leqslant 0$. This translates, for our case of $\varphi = 0^\circ$ and $M_x = 0$, into the continuity from above, $\operatorname{Im}(\Omega) \geqslant 0$, of the cofactor and the determinant at the real Ω -axis. Both functions of Ω are thus extended into the lower half of complex frequencies plane from the values they take above and on the real frequency axis, Appendix J. After this analytic continuation, the zero-pole model, extracted from a 20×20 matrix $t^{min,max}$, is

$$t_{S(0,1),S(0,0)}^{min,max} = 0.053 e^{-2.732i} \frac{f - f_{\text{zero}}}{f - f_{\text{pole}}}, \qquad (97)$$

with frequency, in GHz, given by

$$f_{\text{zero}} = 40.843 + 0.027i$$

 $f_{\text{pole}} = 41.286 - 0.009i$

Following [33], we express the scattering line shape $\left|t_{S(0,1),S(0,0)}^{min,max}\right|^2$ in different forms. The first is

$$\left| t_{S(0,1),S(0,0)}^{min,max} \right|^2 (x) = \rho^2 \frac{(\delta + x)^2 + \gamma^2}{1 + x^2}$$

$$= 2.81 \times 10^{-3} \frac{(-47.47 + x)^2 + 8.55}{1 + x^2},$$
(98)

where $x=-\frac{f-\mathrm{Re}(f_\mathrm{pole})}{\mathrm{Im}(f_\mathrm{pole})},~\delta=-\frac{\mathrm{Re}(f_\mathrm{pole}-f_\mathrm{zero})}{\mathrm{Im}(f_\mathrm{pole})},~\mathrm{and}~\gamma=\frac{\mathrm{Im}(f_\mathrm{zero})}{\mathrm{Im}(f_\mathrm{pole})}.$ The second form is connected with the presence of a continuum background

$$\left| t_{S(0,1),S(0,0)}^{min,max} \right|^2(x) = A_0 + F_0 \frac{(\nu+x)^2}{1+x^2}.$$
 (99)

We found two solutions for the parameters A_0 , F_0 and ν . Namely, $A_0 = 1.06 \times 10^{-5}$, $F_0 = 2.8 \times 10^{-3}$ and $\nu = -47.65$, or $A_0 = 6.37$, $F_0 = -6.36$ and $\nu = 2.09 \times 10^{-2}$. This form is thus ambiguous as is also noted in [33].

The third, and the final format, presents the resonant line shape as a weighted sum of a Fano and Lorentz line shapes

$$\left| t_{S(0,1),S(0,0)}^{min,max} \right|^2(x) = A \left(\eta \frac{(\delta+x)^2}{1+x^2} + (1-\eta) \frac{1}{1+x^2} \right). \tag{100}$$

where the weight parameter is $\eta = 1/(1 + \gamma^2) = 0.105$ and $A = \rho^2(1 + \gamma^2) = 0.027$.

The Fano line shape, which is the first term in (100), contributes 10.5% to the resonance line shape.

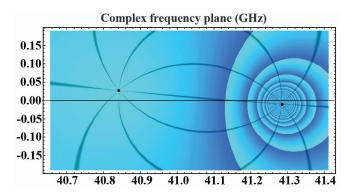


FIG. 21. Representation, in the complex frequency plane, of the scattering matrix element Out S(0,1) at z-min, In S(0,0) at z-max. The closed curves around the pole $41.286-i\ 0.009$, show the absolute value of the scattering matrix as it tends to infinity. The argument of the scattering matrix element is constant on the curves that connect the zero at 40.843+0.027 i with the pole. The real resonant frequency is located above the pole, at 41.286 GHz.

XXIII. CONCLUSION

To sum up, we show how to derive the transfer matrix using Pendry-MacKinnon discrete Maxwell's equations. Space is an orthogonal lattice with lattice constants a, band c on the x, y and z directions, respectively. The z-axis is singled-out as the transfer axis. A finite number of parallel discrete laminae of thickness c are placed perpendicular along the z-axis. Each lamina can carry any non-magnetic, frequency-dependent pattern, independent from each other. The method we introduce computes, in an analytical closed form, the transfer matrix elements for all Bloch-Floquet modes. The computation starts with a large number of path-operators that transfer the field from the first to the last lamina. Fortunately, many of these path-operators come up with a zero contribution and the results of the paths that contribute can be further grouped together in simple terms, which we call channels. Each channel has the interesting attribute of being a product of two terms that bear distinctive features. One term, called the channel's γ -function, depends on the permittivities, whereas the other term, called the channel's \mathcal{Z} -factor, does not. We computed the χ and the \mathcal{Z} -factors for a bilaminar device for all pairs of input output polarization.

To exemplify the building up of a transfer matrix element consider, in continuum case of $a,b\to 0$, the P polarization at the input and the S at the output. The method for the discrete case is similar to the continuum, except that the χ functions are discrete like in (68). For this

(P,S) pair of polarization the transfer matrix element is a sum over 5 channels, having their χ -functions displayed in Fig.22. For Channel 2, as an example, the χ -function is a polynomial in (p_x, p_y) given by $p_y(-\partial_x \epsilon_2) + p_x \partial_y \epsilon_2$, for any permittivity pattern. The transfer matrix elements depend on the Fourier transforms of the χ -functions, which contain all Bloch-Floquet modes through the variable $q_{\perp} = p_{\perp} - p_{\perp}^{\text{OUT}}$. Next, the choice of a pair of \pm propagation direction decides the specific form of the Zfactor. For example, if we are looking for the matrix element $T^{-,-}$, then use Table XI and divide its entries by ||OUT|| to normalize the \mathcal{Z} -factor.

The rule to obtain the \mathcal{Z} -factors for other directions is to change IN- into IN+ and, at the same time, change $\varphi_{z,IN} \to \varphi_{z,IN}^{-1}$, and $c \to -c$, before moving to the cscaled variables. The same rule applies for OUT- into OUT+. However, this rule does not apply for Channel 1, for both SS and PP, for which all unnormalized \mathcal{Z} factors are tabulated in Appendix B Tables VII to XI. Finally, the matrix element is a sum over the product of the Fourier transform of χ and the Z-factor for all channels that belong to the selected polarization pair.

A valuable way of proceeding further is to extend to range of applications. One possibility is to exploit Fig.10 and bring together two devices with distinct number of resonant modes, and examine the propagation along different channels at the interface. Other applications may be connected to metasurfaces [39], energy harvesting [40], [41],[42], leaky-wave theory [42] and frequency-selective surfaces [43].

ACKNOWLEDGMENT

One of us, O.L., wishes to thank the Fulbright Commission for a Fulbright Scholarship grant and the host Victor Lopez-Richard from Universidade Federal de São Carlos, SP, Brazil, where part of this work was done. In addition, O.L. thanks his colleague Mariama Rebello de Sousa Dias for many conversations during the course of this research. Both of us wish to thank Dr. Andrei Silaghi, with Continental Automotive Romania SRL, for facilitating the access to numerical simulation using CST microwave studio [37].

Appendix A: A summary of symbols with explanatory notes

- **1.** The discrete position vectors are $\vec{n} = (an_x, bn_y, cn_z)$ and $n_{\perp} = (an_x, bn_y)$. In the continuous, $a, b \to 0$, the position n_{\perp} becomes $r_{\perp} = (x, y)$.
 - **2.** The vector $p_{\perp} = (p_x, p_y)$ appear in the formulation

of the plane wave basis, $\left|\Psi_{S/P,p_{\perp}}^{\pm}\right\rangle e^{\pm ip_{z}n_{z}c}e^{-i\omega t}$ where $\left|\Psi_{S/P,p_{\perp}}^{\pm}\right\rangle = \left|p_{\perp},S/P,\pm\right\rangle e^{ip_{\perp}n_{\perp}}, (26).$ To distinguish between two Bloch-Floquet modes, one at the input IN and the other one at the output OUT, we write $p_{\perp}^{\rm IN}$ and p_{\perp}^{OUT} , respectively. To keep the final formulas for the transfer matrix elements simple, we use p_{\perp} instead of p_{\perp}^{IN} , as is the case in Fig.6.

- **3.** Connection between p_x and $k_x^E = (ia)^{-1}(e^{iap_x} 1)$,
- **4.** The unitless frequency Ω is defined by $\Omega v_0 = \omega c$,
- **5.** The p_z component appears in $\varphi_z = e^{icp_z}$. $\varphi_z(\zeta) =$ $\zeta - \sqrt{|\zeta^2 - 1|} e^{\frac{i}{2} \left(\arg(\zeta - 1) + \arg(\zeta + 1)\right)}$, (39). The $\arg(\zeta)$ takes values on $[-\pi,\pi)$ in such a way that $\arg(\zeta)=-\pi$ if $\operatorname{Im}(\zeta) = 0$ and $\zeta < 0$. The argument ζ is defined in (38).
- **6.** Periodic boundary conditions introduce the modes (M_x, M_y) and the direction (ξ_x, ξ_y) of the mode (0,0)through (44) and (45).
 - 7. Transfer matrix element $T_{m,n}^{-,-}$ are organized in (50).
 - **8.** All XY-operators are listed in Fig.5.
 - **9.** An example of a discrete χ -function, (68).
 - 10. Discrete Fourier transform of a χ -function, (69).
- 11. The Fourier transform goes from space n_{\perp} to the mode variable $q_{\perp}=p_{\perp}^{\rm IN}-p_{\perp}^{\rm OUT}\equiv p_{\perp}-p_{\perp}^{\rm OUT}.$ 12. An example of a \mathcal{Z} -factor, (71).
- 13. Transfer matrix element as a sum over channels, (72).
- 14. The \mathcal{Z} -factors are tabulated in Table III and VII to XI.
- 15. Rules to obtain all \mathcal{Z} -factors for all directions are presented in Appendix B.
- 16. Some examples of permittivity functions for the continuum (x, y)-plane are in Table IV.
- 17. For the continuum (x, y) case, the χ -functions, the permittivity functions and the polynomial dependence on $p_{\perp} \equiv p_{\perp}^{\rm IN}$ are found in (73), Fig.6 and Fig.22 to 25
- **18.** Through c-scaling, x = cx', y = cy' from (74), the lattice constant c simplifies in the transfer matrix element.
- 19. Choose a unit of length in accordance with the frequency band under study. Use the thickness parameter $t = [1 \text{ unit}](c \text{ [unit]})^{-1}, (78), \text{ to write the transfer}$ matrix element in terms of only unitless parameters.
- 20. Each vertex for any polygonal tessellation pattern carry a pair of orthogonal unit vectors $(\lambda, \hat{\mu})$. An example is the π - π -rig from Fig.7.
- 21. The jumps in the relative permittivities are measured across $\hat{\mu}$ in the direction of $\hat{\lambda}$, (79).
- 22. The Fourier transforms of a tessellated pattern, in continuum, from the position space vector r_{\perp} to the mode vector q_{\perp} , are built on $(\hat{\lambda}, \hat{\mu})$, the permittivities jumps and two constant gauge vector W and \mathcal{D} .

Appendix B: The \mathcal{Z} -factors and the χ -functions

For all tables, $\langle p_{\perp}|p_{\perp}\rangle$ can be written in terms of φ_z through $\langle p_{\perp}|p_{\perp}\rangle c^2\varphi_z = 1 - 2\varphi_z + \Omega^2\varphi_z + \varphi_z^2$. The subscript No. of the XY-operator represents the Channel number.

The Z-factors are valid for both discrete and continuous (x, y)-plane, since they are independent of permittivities.

The χ -functions from Fig.22 to Fig.25 are valid for a continuous (x, y)-plane.

TABLE VII. Unnormalized \mathcal{Z}_1 factor for SS Channel₁

OutS,InS	$\mathcal{Z} ext{-channel}_1 \parallel ext{OUT} \parallel$
-,-	$\frac{i \left\langle p_{\perp}^{\rm OUT} \middle p_{\perp}^{\rm OUT} \right\rangle \left(\left(\Omega^2 \varphi_{z, \rm OUT} + 1 \right)^2 - \varphi_{z, \rm OUT}^2 \right)}{c \varphi_{z, \rm OUT}^4} \delta_{\rm IN, OUT}$
+,-	$-\frac{\imath \Omega^2 \left\langle p_{\perp}^{\rm OUT} \middle p_{\perp}^{\rm OUT} \right\rangle \left(\Omega^2 \varphi_{z, {\rm OUT}} + \varphi_{z, {\rm OUT}}^2 + 1\right)}{c \varphi_{z, {\rm OUT}}} \delta_{\rm IN, {\rm OUT}}$
-,+	$\frac{i\Omega^2 \left\langle p_\perp^{\rm OUT} \middle p_\perp^{\rm OUT} \right\rangle \left(\Omega^2 \varphi_{z,{\rm OUT}} + \varphi_{z,{\rm OUT}}^2 + 1\right)}{c\varphi_{z,{\rm OUT}}} \delta_{\rm IN,OUT}$
+,+	$-\frac{i \left\langle p_{\perp}^{\rm OUT} \middle p_{\perp}^{\rm OUT} \right\rangle \varphi_{z,{\rm OUT}}^2 \left(\left(\varphi_{z,{\rm OUT}} \! + \! \Omega^2 \right)^2 \! - \! 1 \right)}{c} \delta_{\rm IN,OUT}$

The rule to obtain the \mathcal{Z} -factors for other directions is to change IN- into IN+ or OUT- into OUT+ and, at the same time, change $\varphi_{\mathbf{z},\mathrm{IN}} \to \varphi_{\mathbf{z},\mathrm{IN}}^{-1}$ or $\varphi_{\mathbf{z},\mathrm{OUT}} \to \varphi_{\mathbf{z},\mathrm{OUT}}^{-1}$, and $c \to -c$. However, this rule does not apply for Channel 1, for both SS and PP, for which all unnormalized \mathcal{Z} -factors are tabulated in Tables VII and IX. Notice that the lattice constant c is present in these tables to enable the transformation $c \to -c$. The same constant simplifies from the transfer matrix elements after the variables are c-scaled. To normalize the \mathcal{Z} -factors, divide the second column by $\|\mathrm{OUT}\|$, which, by formula (59), can be written in terms of $\varphi_{\mathbf{z},\mathrm{OUT}}$.

TABLE IX. Unnormalized \mathcal{Z}_1 factor for PP Channel₁

OutP,InP	\mathcal{Z} -channel ₁ $\ \mathrm{OUT}\ $
-,-	$-\frac{i \left\langle p_{\perp}^{\rm OUT} \middle p_{\perp}^{\rm OUT} \right\rangle \left(2\Omega^2 \varphi_{z,{\rm OUT}} + \varphi_{z,{\rm OUT}}^2 - 1\right)}{c \varphi_{z,{\rm OUT}}^2} \delta_{\rm IN,OUT}$
+,-	$rac{2i\Omega^2\left\langle p_{\perp}^{ m OUT}\left p_{\perp}^{ m OUT} ight angle arphi_z, m OUT}{c}\delta_{ m IN, m OUT}$
-,+	$-rac{2i\Omega^2\left\langle p_\perp^{ m OUT}\left p_\perp^{ m OUT} ight angle}{carphi_{z, m OUT}}\delta_{ m IN, m OUT}$
+,+	$-\frac{i \left\langle p_{\perp}^{\rm OUT} \middle p_{\perp}^{\rm OUT} \right\rangle \left(-2 \Omega^2 \varphi_{z, {\rm OUT}} + \varphi_{z, {\rm OUT}}^2 - 1\right)}{c} \delta_{\rm IN, {\rm OUT}}$

TABLE XI. Unnormalized \mathcal{Z} factor for OUT S-, IN P-

(XY-operator) _{No.}	$\mathcal{Z}(\text{OUT,S-})(\text{IN,P-}) \parallel \text{OUT} \parallel$
$(\langle T_H \sigma_2 \epsilon_1 T_E \rangle)_1$	$\frac{\Omega^2 \left(\varphi_{z,\mathrm{IN}} - 1\right) \left(\Omega^2 \varphi_{z,\mathrm{OUT}} + 1\right)}{c \varphi_{z,\mathrm{IN}} \varphi_{z,\mathrm{OUT}}^2}$
$(\langle T_H \sigma_2 \epsilon_2 T_E \rangle)_2$	$\frac{\Omega^2 \left(\Omega^2 \varphi_{z,\mathrm{IN}} + \varphi_{z,\mathrm{IN}} - 1\right)}{c \varphi_{z,\mathrm{IN}} \varphi_{z,\mathrm{OUT}}}$
$(\langle T_H \sigma_2 \epsilon_2 T_{\rm E} \rangle \epsilon_1^{-1})_3$	$-\frac{c\Omega^2\left\langle p_\perp^{\rm IN} \middle p_\perp^{\rm IN}\right\rangle}{\varphi_{z,{\rm OUT}}}$
$(\langle T_H \sigma_2 \epsilon_2 T_E \rangle \epsilon_1^{-1} \langle T_E \epsilon_1 $	$(T_E)_4 \qquad \frac{c\Omega^2(\varphi_{z,\text{IN}}-1)}{\varphi_{z,\text{IN}}\varphi_{z,\text{OUT}}}$
$(\langle T_H \sigma_2 \epsilon_2 \epsilon_1 T_E \rangle)_5$	$-\frac{\Omega^4\left(\varphi_{z,\mathrm{IN}}-1\right)}{c\varphi_{z,\mathrm{IN}}\varphi_{z,\mathrm{OUT}}}$

TABLE VIII. Unnormalized \mathcal{Z} factor for OUT P-, IN S-

(XY-operator) _{No.}	$\mathcal{Z}(\text{OUT,P-})(\text{IN,S-}) \parallel \text{OUT} \parallel$
$(\epsilon_1^{-1} \langle T_{\rm E} \epsilon_1 \sigma_2 T_H \rangle)_1$	$-\frac{c \left\langle p_{\perp}^{\text{OUT}} \middle p_{\perp}^{\text{OUT}} \right\rangle}{\varphi_{z, \text{IN}} \varphi_{z, \text{OUT}}}$
$(\epsilon_2^{-1} \left\langle T_{\mathrm{E}} \right \epsilon_1 \sigma_2 \left T_H \right\rangle)_2$	$-\frac{c\left\langle p_{\perp}^{\mathrm{OUT}}\middle p_{\perp}^{\mathrm{OUT}}\right\rangle}{\varphi_{z,\mathrm{IN}}\varphi_{z,\mathrm{OUT}}}$
$(\epsilon_2^{-1} \langle T_{\rm E} \epsilon_2 T_{\rm E} \rangle \epsilon_1^{-1} \langle T_{\rm E} \epsilon_1 \sigma_2 T_{\rm E} \rangle$	$(H)_3 \qquad -\frac{c^3 \langle p_{\perp}^{\text{OUT}} p_{\perp}^{\text{OUT}} \rangle}{\varphi_{z,\text{IN}} \varphi_{z,\text{OUT}}}$
$(\epsilon_2^{-1} \langle T_{\rm E} \epsilon_2 \epsilon_1 \sigma_2 T_H \rangle)_4$	$\frac{c\Omega^2 \left\langle p_{\perp}^{\rm OUT} \middle p_{\perp}^{\rm OUT} \right\rangle}{\varphi_{z,\rm IN} \varphi_{z,\rm OUT}}$
$(\epsilon_2^{-1} raket{T_{ m E} \epsilon_2 \sigma_2 T_H\rangle}_5$	$-\frac{c\left\langle p_{\perp}^{\text{OUT}} \middle p_{\perp}^{\text{OUT}} \right\rangle \left(\Omega^{2} \varphi_{z,\text{IN}} + 1\right)}{\varphi_{z,\text{IN}}^{2} \varphi_{z,\text{OUT}}}$
$(\langle T_E \epsilon_1 \sigma_2 T_H angle)_6$	$\frac{\varphi_{z,\mathrm{OUT}} \!+\! 2\Omega^2 \!-\! 1}{c\varphi_{z,\mathrm{IN}}\varphi_{z,\mathrm{OUT}}}$
$(\langle T_E \epsilon_2 T_E \rangle \epsilon_1^{-1} \langle T_E \epsilon_1 \sigma_2 T_H \rangle)_{7}$	$\frac{c(\varphi_{z,\text{OUT}} + \Omega^2 - 1)}{\varphi_{z,\text{IN}}\varphi_{z,\text{OUT}}}$
$(\langle T_E \epsilon_2 \epsilon_1 \sigma_2 T_H \rangle)_8$	$-\frac{\Omega^2\left(\varphi_{z,\text{OUT}}+\Omega^2-1\right)}{c\varphi_{z,\text{IN}}\varphi_{z,\text{OUT}}}$
$(\langle T_E \epsilon_2 \sigma_2 T_H \rangle)_9$	$\frac{\left(\Omega^2\varphi_{z,\text{IN}}+1\right)\left(\varphi_{z,\text{OUT}}+\Omega^2-1\right)}{c\varphi_{z,\text{IN}}^2\varphi_{z,\text{OUT}}}$

TABLE X. Unnormalized \mathcal{Z} factor for OUT P-, IN P-

(XY-operator) _{No.}	$\mathcal{Z}(\text{OUT,P-})(\text{IN,P-}) \parallel \text{OUT} \parallel$
$(1)_1 \qquad -\frac{i\langle p_{\perp}^{\text{OUT}} p_{\perp}^{\text{OUT}}}{}$	$\frac{\left(2\Omega^2\varphi_{z,\mathrm{OUT}}+arphi_{z,\mathrm{OUT}}^2-1\right)}{carphi_{z,\mathrm{OUT}}^2}\delta_{\mathrm{IN},\mathrm{OUT}}$
$(\epsilon_1^{-1})_2$	$\frac{ic \left\langle p_{\perp}^{\mathrm{IN}} \middle p_{\perp}^{\mathrm{IN}} \right\rangle \left\langle p_{\perp}^{\mathrm{OUT}} \middle p_{\perp}^{\mathrm{OUT}} \right\rangle}{\varphi_{z,\mathrm{OUT}}}$
$(\epsilon_1^{-1} \langle T_{\rm E} \epsilon_1 T_E \rangle)_3$	$-\frac{ic \left\langle p_{\perp}^{\rm OUT} \middle p_{\perp}^{\rm OUT} \right\rangle \left(\varphi_{z,\rm IN} - 1\right)}{\varphi_{z,\rm IN} \varphi_{z,\rm OUT}}$
$(\epsilon_2^{-1})_4$	$\frac{ic \left\langle p_{\perp}^{\rm IN} \left p_{\perp}^{\rm IN} \right\rangle \left\langle p_{\perp}^{\rm OUT} \left p_{\perp}^{\rm OUT} \right\rangle \right.}{\varphi_{z,{\rm OUT}}}$
$(\epsilon_2^{-1} \langle T_{\mathrm{E}} \epsilon_1 T_E \rangle)_5$	$-\frac{ic \left\langle p_{\perp}^{\rm OUT} \middle p_{\perp}^{\rm OUT} \right\rangle \left(\varphi_{z,\rm IN} - 1\right)}{\varphi_{z,\rm IN} \varphi_{z,\rm OUT}}$
$(\epsilon_2^{-1} \langle T_{\rm E} \epsilon_2 T_E \rangle)_6 - \frac{ic\langle r_{\rm E} \rangle}{2}$	$\frac{\left\langle p_{\perp}^{\rm OUT} \middle p_{\perp}^{\rm OUT} \right\rangle \left(\Omega^2 \varphi_{z,\rm IN} + \varphi_{z,\rm IN} - 1\right)}{\varphi_{z,\rm IN} \varphi_{z,\rm OUT}}$
$(\epsilon_2^{-1} \left\langle T_{\mathrm{E}} \right \epsilon_2 \left T_{\mathrm{E}} \right\rangle \epsilon_1^{-1})_7$	$\frac{ic^{3}\left\langle p_{\perp}^{\mathrm{IN}}\left p_{\perp}^{\mathrm{IN}}\right\rangle \left\langle p_{\perp}^{\mathrm{OUT}}\left p_{\perp}^{\mathrm{OUT}}\right\rangle \right.}{\varphi_{z,\mathrm{OUT}}}$
$(\epsilon_2^{-1} \langle T_{\rm E} \epsilon_2 T_{\rm E} \rangle \epsilon_1^{-1} \langle T_{\rm E} \epsilon_2 T_{\rm E} \rangle$	$(T_E)_8 - \frac{ic^3 \langle p_\perp^{\text{OUT}} p_\perp^{\text{OUT}} \rangle (\varphi_{z,\text{IN}} - 1)}{\varphi_{z,\text{IN}} \varphi_{z,\text{OUT}}}$
$(\epsilon_2^{-1} \langle T_{\rm E} \epsilon_2 \epsilon_1 T_E \rangle)_9$	$\frac{ic\Omega^2 \left\langle p_{\perp}^{\rm OUT} \middle p_{\perp}^{\rm OUT} \right\rangle \left(\varphi_{z,\rm IN} - 1\right)}{\varphi_{z,\rm IN} \varphi_{z,\rm OUT}}$
$(\langle T_E \epsilon_1 T_E \rangle)_{10}$	$\frac{i\left(\varphi_{z,\mathrm{IN}}-1\right)\left(\varphi_{z,\mathrm{OUT}}+2\Omega^2-1\right)}{c\varphi_{z,\mathrm{IN}}\varphi_{z,\mathrm{OUT}}}$
$(\langle T_E \epsilon_2 T_E \rangle)_{11}$	$\frac{i\left(\Omega^{2}\varphi_{z,\mathrm{IN}}+\varphi_{z,\mathrm{IN}}-1\right)\left(\varphi_{z,\mathrm{OUT}}+\Omega^{2}-1\right)}{c\varphi_{z,\mathrm{IN}}\varphi_{z,\mathrm{OUT}}}$
$(\langle T_E \epsilon_2 T_{\rm E} \rangle \epsilon_1^{-1})_{12}$	$-\frac{ic\left\langle p_{\perp}^{\rm IN} \left p_{\perp}^{\rm IN} \right\rangle \left(\varphi_{z, \rm OUT} + \Omega^2 - 1\right)}{\varphi_{z, \rm OUT}}$
$(\langle T_E \epsilon_2 T_E \rangle \epsilon_1^{-1} \langle T_E \epsilon_1 T_E \rangle$	(E))13 $\frac{ic(\varphi_{z,\text{IN}}-1)(\varphi_{z,\text{OUT}}+\Omega^2-1)}{\varphi_{z,\text{IN}}\varphi_{z,\text{OUT}}}$
$(\langle T_E \epsilon_2 \epsilon_1 T_E \rangle)_{14}$	$-\frac{i\Omega^2 \left(\varphi_{z,\mathrm{IN}}-1\right) \left(\varphi_{z,\mathrm{OUT}}+\Omega^2-1\right)}{c\varphi_{z,\mathrm{IN}}\varphi_{z,\mathrm{OUT}}}$

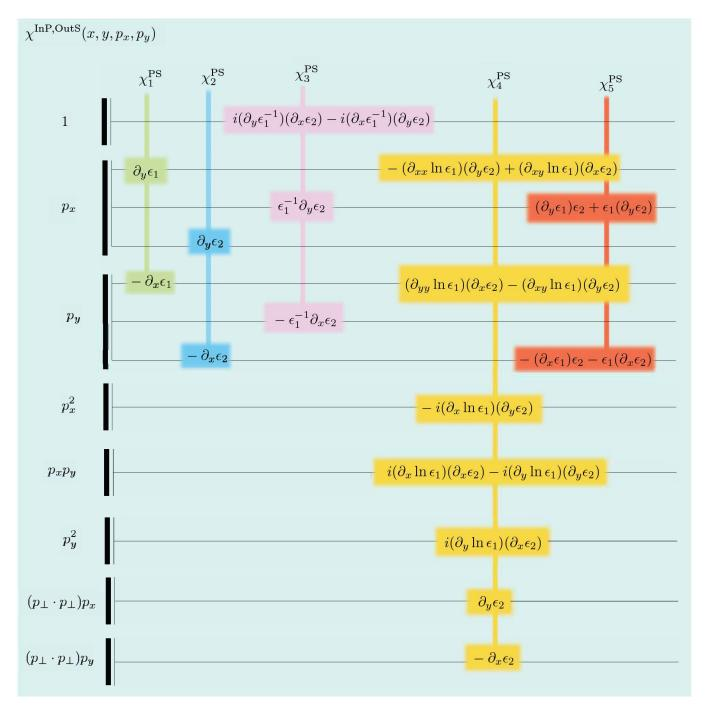


FIG. 22. The χ -functions for the In P Out S channels. From the total of 5 channels, the more elaborate is Channel 4, which is cubic in (p_x, p_y) .

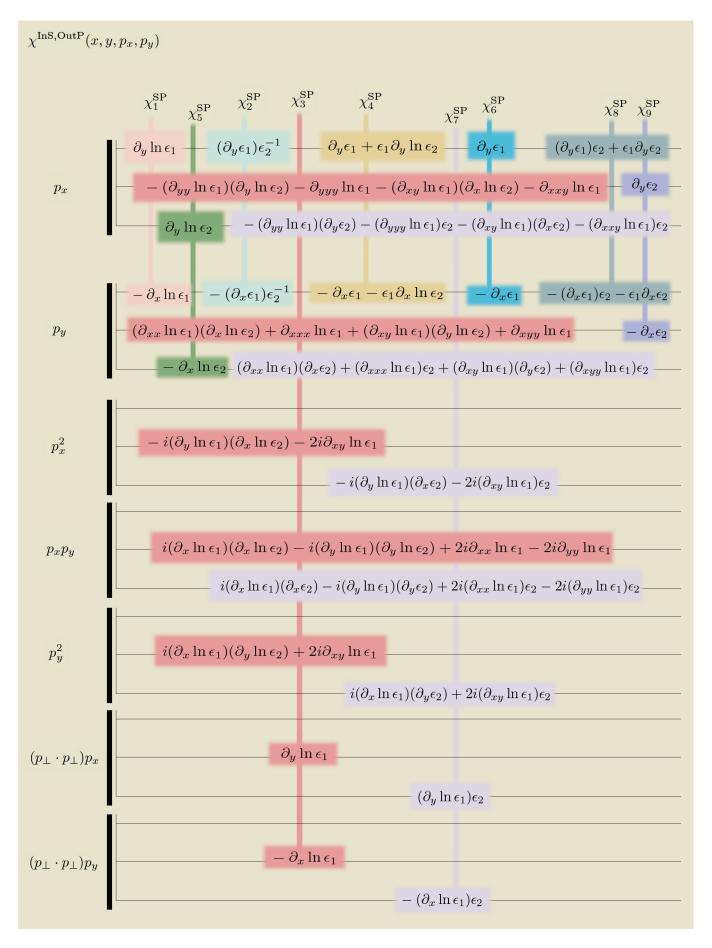


FIG. 23. The χ -functions for the In S Out P channels. From the total of 9 channels, the more elaborate are Channel 3 and 7, which are cubic in (p_x, p_y) .

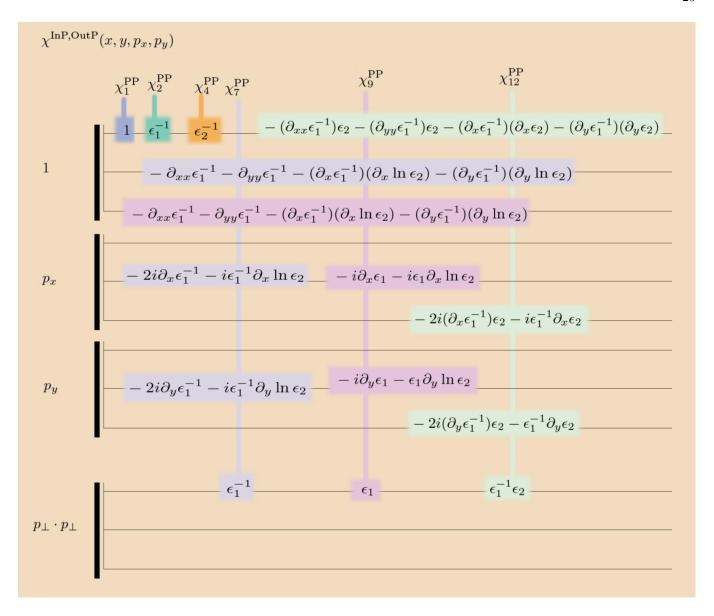


FIG. 24. The χ -functions for the In P Out P channels. This figure contains 6 channels out of the total of 14, which have a nonzero free term as a polynomial in p_x and p_y .

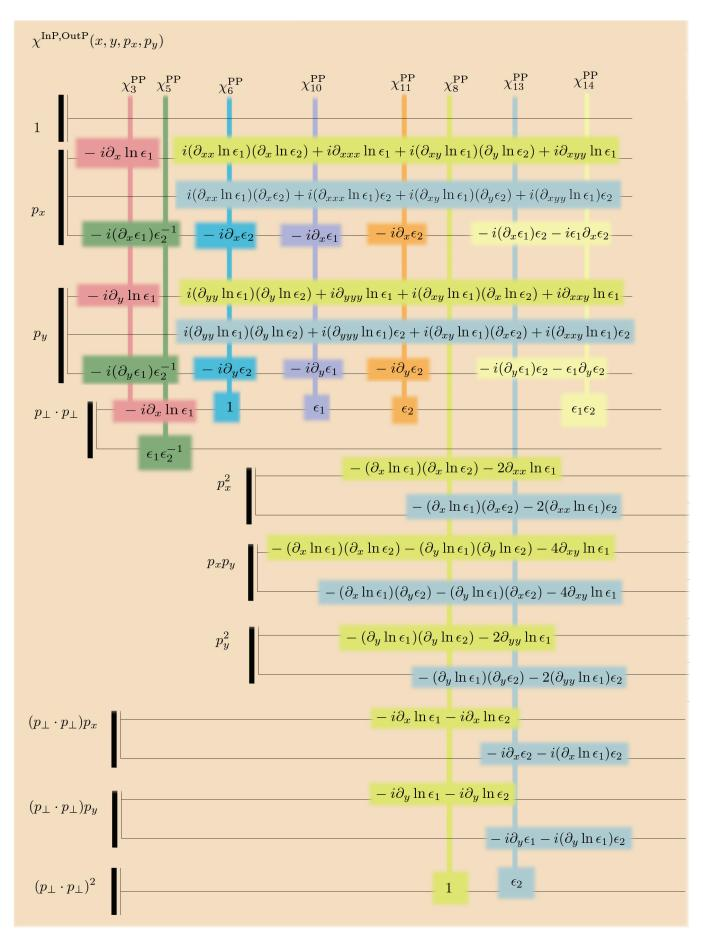


FIG. 25. The χ -functions for the In P Out P channels. This figure contains 8 channels out of the total of 14, which have no free term as a polynomial in p_x and p_y .

Appendix C: The diagonal $T^{-,-}$ matrix elements $(q_{\perp}=0)$ for the π - π -rig and $a,b\to 0$.

$$(T_{Sm,Sm}^{-,-})_{\text{Channel 1}} = -\delta_{\text{IN,OUT}} \frac{\left((\Omega^2 \varphi_{z,\text{OUT}} + 1)^2 - (\varphi_{z,\text{OUT}})^2 \right)}{\left(\varphi_{z,\text{OUT}}^2 - 1 \right) \varphi_{z,\text{OUT}}^3},$$
 (101)

$$(T_{Sm,Sm}^{-,-})_{\text{Channel 2}} = (6\epsilon_{1B} + \epsilon_{1L} + \epsilon_{1R}) \frac{\Omega^2 \left(\Omega^2 \varphi_{z,\text{OUT}} + 1\right)}{8\varphi_{z,\text{IN}} \left(\varphi_{z,\text{OUT}}^2 - 1\right) \varphi_{z,\text{OUT}}},$$
(102)

$$(T_{Sm,Sm}^{--})_{Channel 3} = \frac{\Omega^2}{4\pi^2t^2 (p_x^2 + p_y^2) \varphi_{z,lN} (\varphi_{z,OUT}^2 - 1)}$$

$$\left(p_x^2 \left(\csc(\alpha) \sec(\alpha) \sec(\alpha) \log \left(\epsilon_{1B}\right) + \frac{3}{2} \csc(\alpha) \log \left(\epsilon_{1L}\right) - \ln \left(\epsilon_{1L}\right) - \ln \left(\epsilon_{1R}\right)\right) + \epsilon_{2L} \left(-\csc(\alpha) \sec(\alpha) \log \left(\epsilon_{1B}\right) + \frac{3}{2} \csc(\alpha) \log \left(\epsilon_{1L}\right) - \left(\cot(\alpha) - 2\right) \csc(\alpha) \sec(\alpha) \log \left(\epsilon_{1R}\right)}{2 (\cot(\alpha) + 1)} + \epsilon_{2R} \left(-\csc(\alpha) \sec(\alpha) \log \left(\epsilon_{1B}\right) - \frac{\left(\cot(\alpha) - 2\right) \csc(\alpha) \sec(\alpha) \log \left(\epsilon_{1L}\right)}{2 (\cot(\alpha) + 1)} + \frac{3}{2} \csc(\alpha) \log \left(\epsilon_{1R}\right)\right) + \epsilon_{2R} \left(-\csc(\alpha) \sec(\alpha) \log \left(\epsilon_{1B}\right) - \frac{\csc(\alpha)}{2 (\cot(\alpha) + 1)} + \frac{3}{2} \left(\sin(\alpha) + \cos(\alpha)\right)\right)\right)$$

$$+p_x p_y \frac{\csc(\alpha)}{\sin(\alpha) + \cos(\alpha)} \left(\epsilon_{2L} - \epsilon_{2R}\right) \left(\log \left(\epsilon_{1L}\right) - \log \left(\epsilon_{1R}\right)\right) + p_y^2 \left(\csc(\alpha) \sec(\alpha) \log_2 \left(\epsilon_{1B}\right) - \log \left(\epsilon_{1B}\right) - \log \left(\epsilon_{1L}\right) - \log \left(\epsilon_{1R}\right)\right)\right)$$

$$+\epsilon_{2L} \left(-\csc(\alpha) \sec(\alpha) \log \left(\epsilon_{1B}\right) + \frac{3}{2} \left(\cot(\alpha) + 2\right) \csc(\alpha) \sec(\alpha) \log \left(\epsilon_{1R}\right)}{2 (\cot(\alpha) + 1)} + \epsilon_{2L} \left(-\csc(\alpha) \sec(\alpha) \log \left(\epsilon_{1B}\right) + \frac{3}{2} \left(\cot(\alpha) + 2\right) \csc(\alpha) \sec(\alpha) \log \left(\epsilon_{1R}\right)\right)\right)\right)$$

$$+\epsilon_{2R} \left(-\csc(\alpha) \sec(\alpha) \log \left(\epsilon_{1B}\right) - \frac{\csc(\alpha) \log \left(\epsilon_{1B}\right)}{2 (\sin(\alpha) + \cos(\alpha))} + \frac{3}{2} \left(\cot(\alpha) + 2\right) \csc(\alpha) \sec(\alpha) \log \left(\epsilon_{1R}\right)\right)\right)\right)$$

$$+\epsilon_{2R} \left(-\csc(\alpha) \sec(\alpha) \log \left(\epsilon_{1B}\right) - \frac{\cos(\alpha) \log \left(\epsilon_{1B}\right)}{2 (\sin(\alpha) + \cos(\alpha))} + \frac{3}{2} \left(\cot(\alpha) + 1\right)\right)\right)\right)$$

$$+\epsilon_{2R} \left(-\csc(\alpha) \sec(\alpha) \log \left(\epsilon_{1B}\right) - \frac{\cos(\alpha) \log \left(\epsilon_{1B}\right)}{2 (\sin(\alpha) + \cos(\alpha))} + \frac{3}{2} \left(\cot(\alpha) + 1\right)\right)\right)\right)$$

$$\left(T_{m,m,m}^{--}\right) C_{hannel 4} = -\frac{\Omega^4}{128 \varphi_{z,lN}} \left(\varphi_{z,OUT}^2 - 1\right)$$

$$\left(64\epsilon_{1B}\epsilon_{2B} + 16\epsilon_{1B}\epsilon_{2L} + 16\epsilon_{1B}\epsilon_{2R} + 16\epsilon_{2B}\epsilon_{1L} + 16\epsilon_{2B}\epsilon_{1R} + \frac{4(\cos(\alpha) - \sin(\alpha)) \left(\epsilon_{1L} - \epsilon_{1R}\right) \left(\epsilon_{2L} - \epsilon_{2R}\right)}{\sin(\alpha) + \cos(\alpha)}\right)\right)$$

$$\left(64\epsilon_{1B}\epsilon_{2B} + 16\epsilon_{1B}\epsilon_{2L} + 16\epsilon_{1B}\epsilon_{2R} + 16\epsilon_{2B}\epsilon_{1L} + 16\epsilon_{2B}\epsilon_{1R} + \frac{4(\cos(\alpha) - \sin(\alpha)) \left(\epsilon_{1L} - \epsilon_{1R}\right) \left(\epsilon_{2L} - \epsilon_{2R}\right)}{\sin(\alpha) + \cos(\alpha)}\right)\right)$$

$$\left(64\epsilon_{1B}\epsilon_{2B} + 16\epsilon_{1B}\epsilon_{2L} + 16\epsilon_{2B}\epsilon_{2R} + 16\epsilon_{2B}\epsilon_{1L} + 16\epsilon_{2B}\epsilon_{1R} + \frac{4(\cos(\alpha) - \sin(\alpha)) \left(\epsilon_{1L} - \epsilon_{1R}\right) \left(\epsilon_{2L} - \epsilon_{2R}\right)}{\sin(\alpha) + \cos(\alpha)}\right)\right)$$

$$\left(64\epsilon_{1B}\epsilon_{2B} + 16\epsilon_{1B}\epsilon_{2L} + 16\epsilon_{2B}\epsilon_{2L} + 16\epsilon_{2B}\epsilon_{1L} + 16\epsilon_{2B}\epsilon_{2L}\right)\right)$$

$$\left(64\epsilon_{1B}\epsilon_{2B} + 16\epsilon_{1B}\epsilon_{2L}\right) + \frac{2}{2}\epsilon_{2L}\right)\left(\epsilon_{1B}\epsilon_{2L}\right)\left(\epsilon_{1B}\epsilon_{2L}\right)\left(\epsilon_{1B}\epsilon_{2L}\right)\left(\epsilon_{1B}\epsilon_{2L}\right)\left(\epsilon_{1B}\epsilon_{2L}\right)\left(\epsilon_{1B}\epsilon_{2L}\right)\left(\epsilon_{1B}\epsilon_{2L}\right)\left(\epsilon_{1B}\epsilon_{$$

Appendix D: Fourier transform of a constant function on a polygon. Case $q_{\perp} \neq 0$

Start with the Stokes theorem applied for a polygon in the (x,y)-plane, [36],

$$\iint_{\text{polygon}} (\nabla \times \overrightarrow{F}) \cdot \overrightarrow{dA} = \oint_{\text{right-oriented boundary}} \overrightarrow{F} \cdot \overrightarrow{ds}, \quad (106)$$

where $\overrightarrow{dA} = \hat{z}dxdy$. Take the filed \overrightarrow{F} to be of a special case $\overrightarrow{F}(x,y) = (\hat{z} \times W)e^{q_{\perp} \cdot r_{\perp}}$, with $W = (W_x, W_y)$ a constant 2-dimensional field. Use the right-oriented pair $(\hat{\mu}_j, \hat{\lambda}_j)$ to compute, along each segment of the polygon, the right-hand integral from (106). The integral over each segment gives different results for $q_{\perp} \cdot \hat{\mu}_j \neq 0$ or $q_{\perp} \cdot \hat{\mu}_j = 0$. At this stage in the computations we notice two features (i) the sum over segments is written in terms of sums over vertices, (ii) we can drop the requirement of using a specific orientation of the polygon by using both $\hat{\mu}_j$ and $-\hat{\mu}_j$ for the j^{th} -segment. To accomplish this, if $\hat{\mu}_j$ is associated with the vertex V_j , then associate $-\hat{\mu}_j$ with the vertex V_{j+1} . The result is a vertex-wise formula, with the sum running over the index k that labels the vertices of the polygon

$$\iint_{\text{polygon}} dx dy e^{iq_{\perp} \cdot r_{\perp}} = \sum_{k \in \text{vertices}} \pm \frac{W \cdot \hat{\lambda}_k}{W \cdot q_{\perp}} \frac{1}{q_{\perp} \cdot \hat{\mu}_k} e^{iq_{\perp} \cdot V_k}.$$
(107)

The \pm is the last remnant of the need of an orientation in the Stokes's theorem. To incorporate this \pm into an unoriented polygon, place a permittivity ϵ inside the polygon, $\epsilon = 0$ outside and define the change in ϵ like in (79).

The need for an orientation in the Stokes' theorem is exchange with the need to use a right-oriented pair $(\hat{\mu}, \hat{\lambda})$. This, in turn, imposes the jump to change sign when $\hat{\mu}$ changes sign, which makes the \pm in (107) to become part of $(\Delta \epsilon)_{\hat{\mu}}$. We thus arrived at the formula (81).

Note that the four corners of the unit cell contribute to the (00)-type Fourier integrals. For Channel 1, which is permittivity-independent, the corners contribute with jumps $(\Delta(f_1f_2))_{\hat{\mu}}$ that are equal to ± 1 , given that outside the unit cell we work with $\epsilon = 0$.

Appendix E: Fourier transform of a constant function on a polygon. Case $q_{\perp}=0$

This integral is the area of the polygon, for which a simple answer is given by the sum of the areas of triangles, each triangle producing a term $\frac{1}{2}\hat{z}\cdot(V_{j+1}\times V_j)$. The disadvantage for us is that the vertices V_{j+1} and V_J are not separated, as they are in the formula for $q_{\perp} \neq 0$. Start from (81) and take the limit of $q_{\perp} \rightarrow 0$ along a selected direction \mathcal{D}

$$q_{\perp} = s\mathcal{D} \to 0$$
, as $s \to 0$. (108)

We will show that the final result is independent of the choice of the direction \mathcal{D} . With this choice of q_{\perp} and

 $\mathcal{D} \cdot \hat{\mu} \neq 0$ for all $\hat{\mu}$, formula (81) becomes

$$\sum_{\text{vertices}} e^{i\mathcal{D}\cdot Vs} \sum_{\hat{\mu}_{\text{vertex}}} \frac{W \cdot \hat{\lambda}}{W \cdot \mathcal{D}} \frac{1}{s} (-\Delta \epsilon)_{\hat{\mu}} \frac{1}{\mathcal{D} \cdot \hat{\mu}} \frac{1}{s} . \quad (109)$$

In (109) there is a second-order singularity, s^{-2} , which we need to eliminate. To do just that, expand the exponential in Taylor series and examine the terms that belong to $\hat{\mu}$ and $-\hat{\mu}$ oriented along the same edge and notice that the second-order singularity is eliminated. However, a first-order singularity s^{-1} came into being. This singularity goes away too once we sum up its contribution along a closed loop. Once the singularity s^{-1} is eliminated, we are left, in the limit $s \to 0$, with one term per segment

$$\frac{W \cdot \hat{\lambda}_j}{W \cdot \mathcal{D}} \frac{1}{\mathcal{D} \cdot \hat{\mu}_j} (-\Delta \epsilon)_{\hat{\mu}_j} \frac{1}{2} \left((i\mathcal{D} \cdot V_j)^2 - (i\mathcal{D} \cdot V_{j+1})^2 \right). \tag{110}$$

This term can be placed back into a format that contains two $\hat{\mu}$ vectors per each edge. This is the result (82).

We prove that the result thus obtained is independent on the choice of W and \mathcal{D} by showing that (82) is equal to sum of areas of triangles. Call the vertices of the jedge by V_j and V_{j+1} . Placed at V_j and V_{j+1} are $(\hat{\lambda}_j, \hat{\mu}_j)$ and $(\hat{\lambda}_{j+1}, \hat{\mu}_{j+1}) = (-\hat{\lambda}_j, -\hat{\mu}_j)$, respectively. Along the computation we use $V_{j+1} - V_j = \hat{\mu}_j l_j$, where l_j is the length of the edge. Change the dot product into a cross product, $W \cdot \hat{\lambda} = (\hat{z} \times W) \cdot \hat{\mu}$, to prove the equality

$$\frac{W \cdot \hat{\lambda}_{j}}{W \cdot \mathcal{D}} \frac{1}{\mathcal{D} \cdot \hat{\mu}_{j}} (-\Delta \epsilon)_{\hat{\mu}_{j}} \frac{1}{2} (i\mathcal{D} \cdot V_{j})^{2} + \frac{W \cdot \hat{\lambda}_{j+1}}{W \cdot \mathcal{D}} \frac{1}{\mathcal{D} \cdot \hat{\mu}_{j+1}} (-\Delta \epsilon)_{\hat{\mu}_{j+1}} \frac{1}{2} (i\mathcal{D} \cdot V_{j+1})^{2} = (111)$$

$$(-\Delta \epsilon)_{\hat{\mu}_{j}} \frac{1}{W \cdot \mathcal{D}} \frac{1}{2} (\hat{z} \times W) \cdot \left(\frac{V_{j+1} - V_{j}}{l_{j}} (\mathcal{D} \cdot V_{j}) + \frac{V_{j+1} - V_{j}}{l_{j}} (\mathcal{D} \cdot V_{j+1}) \right) l_{j} .$$

There are four terms in the last line of (111). Two out of these four sum up to zero when we go around a closed loop keeping in mind that $(-\Delta\epsilon)_{\hat{\mu}_j}$ is the same for all $\hat{\mu}_j$ because we are working for a polygon with one kind of permittivity inside and $\epsilon = 0$ outside.

We are left with the sum of the other two terms, which, by the Binet-Cauchy vector relation, is transformed into a sum of oriented areas of triangles OV_jV_{j+1} , where O is some arbitrary origin.

Appendix F: The integral (00) on a polygonal tessellation of the plane In the tessellated plane, for a selected vertex V and a pair $(\hat{\lambda}, \hat{\mu})$ associated with this vertex, there are exactly two contributions from the two polygons that have a common edge along $\hat{\mu}$. Two permittivity jumps along $\hat{\mu}$ originate from these two distinct polygons, each polygon being surrounded by a medium

with $\epsilon = 0$. The sum of these polygonal jumps is actually equal to $(-\Delta(f_1f_2))_{\hat{\mu}}$ but on the tessellated structure. We arrived at the formula for the polygonal tessellation (81).

Appendix G: Translation of a virtual point

A virtual point appears at the intersection of a line from plane 1 and another line from plane 2, which are described by $r_1 = V_{12} + \mu_1 \hat{\mu}_1$ and $r_2 = V_{12} + \mu_2 \hat{\mu}_2$, respectively. Parameters μ_1 and μ_2 run on the real axis. Apply a translation in plane 1, $\delta r_1 = (\delta x_1, \delta y_1)$, and plane 2, $\delta r_2 = (\delta x_2, \delta y_2)$, respectively. Written in terms of a new set of parameters, μ_1 and μ_2 , the translated lines are

$$(r_1)_{\text{translated}} = V_{12} - (\delta r_1 \cdot \hat{\lambda}_1) \hat{\lambda}_1 + \mu_1' \hat{\mu}_1,$$

$$(r_2)_{\text{translated}} = V_{12} - (\delta r_2 \cdot \hat{\lambda}_2) \hat{\lambda}_2 + \mu_2' \hat{\mu}_2.$$
(112)

To compute the position of the translated intersection, $(V_{12})_{\text{translated}}$, solve for μ'_1 and μ'_2 such that $(r_1)_{\text{translated}} = (r_2)_{\text{translated}}$. Use $\hat{\mu}_2 \cdot \hat{\lambda}_1 = -\hat{\mu}_1 \cdot \hat{\lambda}_2$ and get at the final result (85).

Appendix H: Fourier transforms for product of derivatives of type (01), (10) and (11)

We expand on (88) and (89). In order to simplify the computation of $\partial_{\delta x_1}$ and others of this kind, for case (2), (i.e. $q_{\perp} \cdot \hat{\mu} = 0$ and $q_{\perp} \neq 0$), compound the product of the two vertex-dependent terms in one exponential

$$e^{iq_{\perp}\cdot V}(i\hat{\mu}\cdot V) = \frac{d}{ds}\left(e^{iq_{\perp}\cdot V + si\hat{\mu}\cdot V}\right)|_{s=0}. \tag{113}$$

For case (3), $q_{\perp} = 0$, in a similar way as above, we get

$$\frac{1}{2}(i\mathcal{D} \cdot V)^2 = \frac{1}{2} \left(\frac{d^2}{ds^2}\right)_{s=0} e^{i(\mathcal{D} \cdot V)s}.$$
 (114)

To group together the results for case (1) and (3), we found it useful to define a function $e^{i(q_{\perp} \cdot V)_m}$, which for $q_{\perp} \neq 0$ it is equal to $e^{iq_{\perp} \cdot V}$. For $q_{\perp} = 0$ and for any natural number m it is $\frac{1}{2} \left(\frac{d^2}{ds^2} \right)_{s=0} \left(e^{i(\mathcal{D} \cdot V)s} s^m \right)$. So

$$e^{i(q_{\perp} \cdot V)_{m}} = \begin{cases} e^{i(q_{\perp} \cdot V)} & \text{for all } m, \text{if } q_{\perp} \neq 0, \\ \frac{1}{2} (i\mathcal{D} \cdot V)^{2} & \text{if } m = 0, \text{and } q_{\perp} = 0, \\ i\mathcal{D} \cdot V & \text{if } m = 1, \text{and } q_{\perp} = 0, \\ 1 & \text{if } m = 2, \text{and } q_{\perp} = 0, \\ 0 & \text{if } m \geqslant 3, \text{and } q_{\perp} = 0. \end{cases}$$
(115)

The function, for $q_{\perp} = 0$, is equal to the term number 2 - m, from the Taylor expansion.

With the help of this function, the contribution to the type (10)-integral, Section XVI, from a pair from plane 1, i.e. $(V_1, \hat{\mu})$, is

$$e^{i(\mathcal{D}\cdot V_1)_{m_x^1 + m_y^1}} (-i\mathcal{D}_x)^{m_x^1} (-i\mathcal{D}_y)^{m_y^1}$$

$$\frac{W\cdot \hat{\lambda}}{W\cdot \mathcal{D}} (-\Delta (f_1 f_2)_{\hat{\mu}}) \frac{1}{\mathcal{D}\cdot \hat{\mu}},$$
(116)

where \mathcal{D} is arbitrary, subject to the condition that $\mathcal{D} \cdot \hat{\mu} \neq 0$ for all $\hat{\mu}$ in plane 1. The contribution to the type (01)-integral from all real points from plane 2, i.e. V_2 , is a mirror image.

The contribution to the type (11)-integral from a virtual point, V_{12} , under constrained translation has a different aspect, being

$$\sum_{\text{all four } \hat{\mu}' \text{s}} e^{i(\mathcal{D} \cdot V_{12})_{m_{x}^{1} + m_{y}^{1} + m_{x}^{2} + m_{y}^{2}}}$$

$$(\lambda_{1x})^{m_{x}^{1}} (\lambda_{1y})^{m_{y}^{1}} (\lambda_{2x})^{m_{x}^{2}} (\lambda_{2y})^{m_{y}^{2}}$$

$$\left(i \frac{\mathcal{D} \cdot \hat{\mu}_{2}}{\hat{\mu}_{1} \cdot \hat{\lambda}_{2}}\right)^{m_{x}^{1} + m_{y}^{1}} \left(i \frac{\mathcal{D} \cdot \hat{\mu}_{1}}{\hat{\mu}_{2} \cdot \hat{\lambda}_{1}}\right)^{m_{x}^{2} + m_{y}^{2}}$$

$$\frac{W \cdot \hat{\lambda}}{W \cdot \mathcal{D}} (-\Delta (f_{1}f_{2})_{\hat{\mu}}) \frac{1}{\mathcal{D} \cdot \hat{\mu}} .$$

$$(117)$$

To avoid carrying over a minus sign and to arrive at the above formula, we use $\hat{\mu}_2 \cdot \hat{\lambda}_1 = -\hat{\mu}_1 \cdot \hat{\lambda}_2$. The sum, for a fixed virtual point V_{12} , is over all four $\hat{\mu}$'s, which have the tail located at V_{12} .

The above sum, if needed, can be place in a form which is independent of the gauge vector W. For that, first notice that

$$(\lambda_{1x})^{m_x^1} (\lambda_{1y})^{m_y^1} (\lambda_{2x})^{m_x^2} (\lambda_{2y})^{m_y^2}$$

$$\left(i \frac{\mathcal{D} \cdot \hat{\mu}_2}{\hat{\mu}_1 \cdot \hat{\lambda}_2} \right)^{m_x^1 + m_y^1} \left(i \frac{\mathcal{D} \cdot \hat{\mu}_1}{\hat{\mu}_2 \cdot \hat{\lambda}_1} \right)^{m_x^2 + m_y^2}$$

$$(118)$$

is the same for all four $\hat{\mu}$'s, which have the tail located at V_{12} .

Second, use the relation

$$\sum_{\text{all four } \hat{\mu}' \text{s}} \frac{W \cdot \hat{\lambda}}{W \cdot \mathcal{D}} (-\Delta (f_1 f_2)_{\hat{\mu}}) \frac{1}{\mathcal{D} \cdot \hat{\mu}} = \frac{\left| \hat{\lambda}_1 \cdot \hat{\mu}_2 \right|}{(\mathcal{D} \cdot \hat{\mu}_1)(\mathcal{D} \cdot \hat{\mu}_2)} (\Delta f)_{\hat{\mu}_1} (\Delta g)_{\hat{\mu}_2}$$
(119)

valid for any two choices of $\hat{\mu}_1$ and $\hat{\mu}_2$, which have the tail located at V_{12} and the tip on line 1 and line 2, respectively.

The contribution of a virtual point can be thus brought into a W-independent form

$$\sum_{V_{12},\text{two }\hat{\mu}'\text{s}} e^{i(\mathcal{D}\cdot V_{12})_{m_x^1 + m_y^1 + m_x^2 + m_y^2}}$$

$$\left(i\frac{\mathcal{D}\cdot\hat{\mu}_2}{\hat{\mu}_1\cdot\hat{\lambda}_2}\lambda_{1x}\right)^{m_x^1} \left(i\frac{\mathcal{D}\cdot\hat{\mu}_2}{\hat{\mu}_1\cdot\hat{\lambda}_2}\lambda_{1y}\right)^{m_y^1}$$

$$\left(i\frac{\mathcal{D}\cdot\hat{\mu}_1}{\hat{\mu}_2\cdot\hat{\lambda}_1}\lambda_{2x}\right)^{m_x^2} \left(i\frac{\mathcal{D}\cdot\hat{\mu}_1}{\hat{\mu}_2\cdot\hat{\lambda}_1}\lambda_{2y}\right)^{m_y^2}$$

$$\frac{\left|\hat{\lambda}_1\cdot\hat{\mu}_2\right|}{(\mathcal{D}\cdot\hat{\mu}_1)(\mathcal{D}\cdot\hat{\mu}_2)} (\Delta f)_{\hat{\mu}_1}(\Delta g)_{\hat{\mu}_2}.$$

$$(120)$$

To show (119), choose two out of four vectors that have the tail on the virtual point and direction on the line in plane 1 and plane 2, and call them $\hat{\mu}_1$ and $\hat{\mu}_2$, respectively. The other two vectors are $-\hat{\mu}_1$ and $-\hat{\mu}_2$. Use

$$-\Delta(f_1 f_2)_{\hat{\mu}_1} - \Delta(f_1 f_2)_{-\hat{\mu}_1} = -(-\Delta(f_1 f_2)_{\hat{\mu}_2} - \Delta(f_1 f_2)_{-\hat{\mu}_2})$$
(121)

and get

$$\sum_{\text{all four } \hat{\mu}' \text{s}} \frac{W \cdot \hat{\lambda}}{W \cdot \mathcal{D}} (-\Delta (f_1 f_2)_{\hat{\mu}}) \frac{1}{\mathcal{D} \cdot \hat{\mu}} = \left(\frac{W \cdot \hat{\lambda}_1}{W \cdot \mathcal{D}} \frac{1}{\mathcal{D} \cdot \hat{\mu}_1} - \frac{W \cdot \hat{\lambda}_2}{W \cdot \mathcal{D}} \frac{1}{\mathcal{D} \cdot \hat{\mu}_2} \right)$$

$$(-\Delta (f_1 f_2)_{\hat{\mu}_1} - \Delta (f_1 f_2)_{-\hat{\mu}_1}).$$
(122)

A vector identity, valid for any W, \mathcal{D} and two pairs $(\hat{\lambda}_1, \hat{\mu}_1)$ and $(\hat{\lambda}_2, \hat{\mu}_2)$,

$$(W \cdot \hat{\lambda}_1)(\mathcal{D} \cdot \hat{\mu}_2) - (W \cdot \hat{\lambda}_2)(\mathcal{D} \cdot \hat{\mu}_1) = (W \cdot \mathcal{D})(\hat{\lambda}_1 \cdot \hat{\mu}_2) \quad (123)$$

brings the right-hand side of (122) into the form

$$\left(\frac{\hat{\lambda}_1 \cdot \hat{\mu}_2}{(\mathcal{D} \cdot \hat{\mu}_1)(\mathcal{D} \cdot \hat{\mu}_2)}\right) \left(-\Delta (f_1 f_2)_{\hat{\mu}_1} - \Delta (f_1 f_2)_{-\hat{\mu}_1}\right). (124)$$

The final step is to prove that

$$(-\Delta(f_1 f_2)_{\hat{\mu}_1} - \Delta(f_1 f_2)_{-\hat{\mu}_1})(\hat{\lambda}_1 \cdot \hat{\mu}_2) = (\Delta f_1)_{\hat{\mu}_1} (\Delta f_2)_{\hat{\mu}_2} |\hat{\lambda}_1 \cdot \hat{\mu}_2|.$$
(125)

This last equality can be established by going through every of the four cases of pairs $(\hat{\lambda},\hat{\mu})$. Another way is to notice that $-\Delta(f_1f_2)_{\hat{\mu}_1} - \Delta(f_1f_2)_{-\hat{\mu}_1}$ is equal to $(\Delta f)_{\hat{\mu}_1}(\Delta g)_{\hat{\mu}_2}$ up to a sign, i.e. $-\Delta(f_1f_2)_{\hat{\mu}_1} - \Delta(f_1f_2)_{-\hat{\mu}_1} = \pm(\Delta f_1)_{\hat{\mu}_1}(\Delta f_2)_{\hat{\mu}_2}$. This is so, because the left-hand side is invariant under the change in sign $\hat{\mu}_1 \to -\hat{\mu}_1$, whereas the right-hand side changes its sign. The absolute value eliminates this change in sign and so the equality is valid.

Appendix I: The optimization procedure for selecting the dielectric constants

Construct, out of (52), a 8 × 5 sub-matrix composed of transfer matrix elements that couples only the S-polarization of the four modes selected, (0,0), (-1,0), (0,-1), (0,1). The equations to solve are obtained from formula (49). The OUT set (DIR,POL,BF) is composed of (\pm,S,m) , with $m=1,\ldots,4$ from Table XII. Given the absence of any source at $z=+\infty$, the coefficients $C_{\rm POL,BF}^{\rm DIR}$ are all zero for $(-,S,m), m=1,\ldots,4$. At IN, the set (dir,pol,bf) contains the incoming (+,S,1) and the reflected (-,S,m), with $m=1,\ldots,4$. There are 8 unknown coefficients, 4 at OUT and another 4 at IN.

TABLE XII. Mode ordering and Rayleigh frequency for $\theta=17.5^{\circ}$ and $\varphi=0^{\circ}$

(M_x, M_y)	m	Pol.,m	$f_R[\mathrm{GHz}]$
(0,0)	1	S1=S(0,0), P1=P(0,0)	0.0
(-1,0)	2	S2=S(-1,0), P2=P(-1,0)	36.6827
(0,-1)	3	S3=S(0,-1), P3=P(0,-1)	50.0289
(0,1)	4	S4=S(0,1), P4=P(0,1)	50.0289
(-1,-1)	5	S5=S(-1,-1), P5=P(-1,-1)	56.7146
(-1,1)	6	S6=S(-1,1), P6=P(-1,1)	56.7146
(1,0)	7	S7=S(1,0), P7=P(1,0)	68.23087
(-2,0)	8	S8=S(-2,0), P8=P(-2,0)	73.36548
(-2,-1)	9	S9=S(-2,-1), P9=P(-2,-1)	84.68336
(-2,1)	10	S10=S(-2,1), P10=P(-2,1)	84.68336

^a The odd and even Polarization-Bloch-Floquet No., in column 3, corresponds to the S and P polarization, respectively. It is easier to use the index that runs from 1 to 20 in columns 3, when working with a 20×20 matrix. However, to associate a meaning to the Polarizatio-Bloch-Floquet No., the other two styles shown in column 3 may be better.

The 8×5 matrix transfers the input column vector $(\mathcal{C}_{S1}^+, \mathcal{C}_{S1}^-, \mathcal{C}_{S2}^-, \mathcal{C}_{S3}^-, \mathcal{C}_{S4}^-)$ into the output $(C_{S1}^+, C_{S2}^+, C_{S3}^+, C_{S4}^+, 0, 0, 0, 0)$. For ease of reading, the IN and OUT coefficients are marked using distinct Within this approximation, we can solve 8 equations for 8 unknowns coefficients, by fixing the input $\mathcal{C}_{S1}^+ = 1$. The coefficients thus found are the transmission and reflection coefficients for the 4 modes under consideration. To construct an objective function for the optimization process we use a series of properties. The first property is that in the vicinity of the resonant frequency the absolute value of the determinant of the 4×4 matrix $(T_{Sm,Sn}^{-,-})$ attains a minimum. The second one is that the absolute value of the transmission and reflection coefficients of the evanescent modes need to attain high values. The third property is based on the absorptance factor defined as $1 - |C_{S1}^+|^2 - |C_{S2}^+|^2 - |\boldsymbol{\mathcal{C}}_{S1}^-|^2 - |\boldsymbol{\mathcal{C}}_{S2}^-|^2$, similarly to the definition from [44]. The absorptance factor goes through a maximum around the resonant frequency. The objective function we use is

$$\left| Det(T_{Sm,Sn}^{-,-}) \right| +$$

$$\left| \left| C_{S1}^{+} \right|^{2} + \left| C_{S2}^{+} \right|^{2} + \left| \mathcal{C}_{S1}^{-} \right|^{2} + \left| \mathcal{C}_{S2}^{-} \right|^{2} - 0.5 \right|$$

$$+ \left| \left| C_{S2}^{+} \right| - 10 \right| + \left| \left| C_{S4}^{+} \right| - 10 \right| .$$
(126)

Only the transmission coefficients for the evanescent waves are present in (126) because we expect that the reflection coefficients be very close, in absolute value, to the transmission values. We choose 10 as a target number for this values. For the absorptance factor the target values is chosen at 0.5.

For a fixed frequency in the range 37 GHz to 50 GHz, we found a local minimum for this objective function in the 6-dimensional space of the dielectric constants, each constant constrained to be between 1 and 12. After scan-

ning 100 frequencies, the local minimum we selected has f=41.29 GHz, $Det(T_{Sm,Sn}^{-,-})=2.5\times 10^{-5}-3.7\times 10^{-5}i$, $C_{S1}^+=0.59-0.0022i$, $\mathcal{C}_{S1}^-=-0.21-0.59i$, $C_{S2}^+=0.041+0.31i$, $\mathcal{C}_{S2}^-=0.04+0.34i$, $C_{S3}^+=-10.03-0.15i$, $\mathcal{C}_{S3}^-=-10.61-0.18i$, $C_{S4}^+=-3.92+9.20i$ and $\mathcal{C}_{S4}^-=-4.13+9.74i$. We see that the obtained determinant is a small number and that the reflection and the transmissions coefficients are close, in absolute value, to the value 10 we imposed. The absorptance factor came out as 0.04, far from the value of 0.5. This is because in the vicinity of the resonant frequency the transmission and reflection coefficients of the propagative modes attain a minimum at frequencies slightly different than the resonance. The dielectric permittivity set for the local minimum is

$$\epsilon_{1B} = 4.98655, \epsilon_{2B} = 2.95855, \epsilon_{1L} = 7.59549,$$

$$\epsilon_{2L} = 5.663, \epsilon_{1R} = 5.92965, \epsilon_{2R} = 1.63434$$
(127)

Appendix J: Complex frequency plane

The real resonant frequency is located at the minimum of the determinant on the real Ω -axis. The zero of the cofactor is located in the upper complex plane, $\text{Im}(f_{zero}) > 0$. A search for the minimum of the absolute

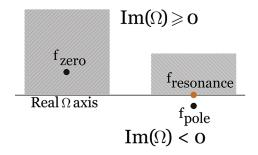


FIG. 26. The domain used for the cofactor surrounds the zero f_{zero} . The domain for determinant does not contain f_{pole} , but it contains the resonant frequency. Both domains are above the real Ω axis

value of the Cofactor_{S(0,0),S(0,1)} ($T^{-,-}$) gives a complex frequency $\Omega_{zero}=0.213999052599+0.00014322547392i$, for which the Cofactor attains the value of $-4.17186\times 10^{-7}+5.51181\times 10^{-7}i$. Translated in frequency, using c=0.25mm, we get $f_{zero}=40.8425+0.0273351i$ in GHz. Once this zero is localized, the parameters a and b are estimated through a linear regression, [38].

The linear approximation of the cofactor in the vicinity of Ω_{zero} ,

$$Cofactor_{S(0,0),S(0,1)}(T^{-,-}) \cong (a+ib)(\Omega - \Omega_{zero}), (128)$$

contains two unknown parameters, a and b. The numerical data consists of pairs $(\Omega, \operatorname{Cofactor}_{S(0,0),S(0,1)}(T^{-,-}))$ obtained from sampling the upper complex-frequency plane using the analytical formulas for the transfer matrix.

The linear approximation for the determinant starts with localizing $Re(\Omega_{resonance}) = 0.21632449245970709$

on the real axis at the point where the absolute value of the determinant becomes minimum, attaining the value 1.15869. In terms of the frequency, the resonance is at $\text{Re}(f_{resonance}) = 41.28635279688047$ GHz. The linear approximation of the determinant in the vicinity of $\Omega_{pole} = 0.21632449245970709 + iy_{pole}$,

$$Det(T^{-,-}) \cong (a' + ib')(\Omega - \Omega_{pole}),$$
 (129)

contains three unknown parameters, $a^{'}$, $b^{'}$ and y_{pole} . The numerical data consists of pairs $(\Omega, Det(T^{-,-}))$ obtained from sampling the upper complex-frequency plane around $Re(\Omega_{resonance})$ using the analytical formulas for the transfer matrix. The fit this time is nonlinear because of the product $(a^{'}+ib^{'})y_{pole}$.

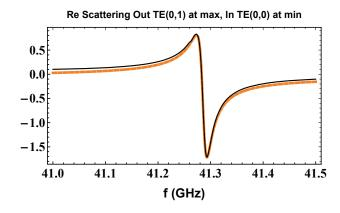


FIG. 27. The real part of the scattering matrix element. The dashed curve (orange) is the zero-pole approximation, whereas the continuous curve (black) is derived from the 20 by 20 transfer matrix using the first 10 Rayleigh-ordered modes.

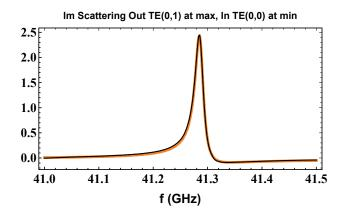


FIG. 28. The imaginary part of the scattering matrix element. The dashed curve (orange) is the zero-pole approximation, whereas the continuous curve (black) is derived from the 20 by 20 transfer matrix using the first 10 Rayleigh-ordered modes.

- J. Xiong, E.-L. Hsiang, Z. He, T. Zhan, and S.-T. Wu, Augmented reality and virtual reality displays: emerging technologies and future perspectives, Light: Science & Applications 10, 1 (2021).
- [2] B. C. Kress and I. Chatterjee, Waveguide combiners for mixed reality headsets: a nanophotonics design perspective, Nanophotonics 10, 41 (2021).
- [3] N. Shlezinger, G. C. Alexandropoulos, M. F. Imani, Y. C. Eldar, and D. R. Smith, Dynamic metasurface antennas for 6g extreme massive mimo communications, IEEE Wireless Communications 28, 106 (2021).
- [4] J. Lorenzo, A. Lázaro, R. Villarino, and D. Girbau, Modulated frequency selective surfaces for wearable rfid and sensor applications, IEEE Transactions on Antennas and Propagation 64, 4447 (2016).
- [5] E. Descrovi, T. Sfez, M. Quaglio, D. Brunazzo, L. Dominici, F. Michelotti, H. P. Herzig, O. J. Martin, and F. Giorgis, Guided bloch surface waves on ultrathin polymeric ridges. Nano letters 10, 2087 (2010).
- [6] P. Lova, G. Manfredi, and D. Comoretto, Advances in functional solution processed planar 1d photonic crystals, Advanced Optical Materials 6, 1800730 (2018).
- [7] R. P. Feynman, Simulating physics with computers, in Feynman and computation (CRC Press, 2018) pp. 133– 153
- [8] A. Hagar, Discrete or continuous?: the quest for fundamental length in modern physics (Cambridge University Press, 2014).
- [9] N. E. Nörlund, Vorlesungen über differenzenrechnung, Vol. 13 (J. Springer, 1924).
- [10] F. Nijhoff and H. Capel, The discrete korteweg-de vries equation, Acta Applicandae Mathematica 39, 133 (1995).
- [11] M. J. Feigenbaum, Quantitative universality for a class of nonlinear transformations, Journal of statistical physics 19, 25 (1978).
- [12] P. Cvitanović, Universality in chaos, in *Universality in chaos* (Routledge, 2017) pp. 3–34.
- [13] B. B. Mandelbrot and B. B. Mandelbrot, The fractal geometry of nature, Vol. 1 (WH freeman New York, 1982).
- [14] D. J. Korteweg and G. De Vries, Xli. on the change of form of long waves advancing in a rectangular canal, and on a new type of long stationary waves, The London, Edinburgh, and Dublin Philosophical Magazine and Journal of Science 39, 422 (1895).
- [15] R. Hirota, Nonlinear partial difference equations iii; discrete sine-gordon equation, Journal of the Physical Society of Japan 43, 2079 (1977).
- [16] R. Hirota, Discrete analogue of a generalized toda equation, Journal of the Physical Society of Japan 50, 3785 (1981).
- [17] I. Krichever, O. Lipan, P. Wiegmann, and A. Zabrodin, Quantum integrable models and discrete classical hirota equations, Communications in Mathematical Physics 188, 267 (1997).
- [18] O. Lipan, P. B. Wiegmann, and A. Zabrodin, Fusion rules for quantum transfer matrices as a dynamical system on grassmann manifolds, Modern Physics Letters A 12, 1369 (1997).
- [19] J. Pendry and A. MacKinnon, Calculation of photon dispersion relations, Physical Review Letters 69, 2772 (1992).

- [20] J. Pendry, Photonic band structures, Journal of Modern Optics 41, 209 (1994).
- [21] J. Pendry and P. Bell, Transfer matrix techniques for electromagnetic waves, in *Photonic Band Gap Materials* (Springer, 1996) pp. 203–228.
- [22] Z.-Y. Li and L.-L. Lin, Photonic band structures solved by a plane-wave-based transfer-matrix method, Physical Review E 67, 046607 (2003).
- [23] L. L. Sánchez-Soto, J. J. Monzón, A. G. Barriuso, and J. F. Cariñena, The transfer matrix: A geometrical perspective, Physics Reports 513, 191 (2012).
- [24] D. Rhazi and N. Atalla, A simple method to account for size effects in the transfer matrix method, The journal of the acoustical society of america 127, EL30 (2010).
- [25] P. Yeh, A. Yariv, and C.-S. Hong, Electromagnetic propagation in periodic stratified media. i. general theory, JOSA 67, 423 (1977).
- [26] S. Fan, Sharp asymmetric line shapes in side-coupled waveguide-cavity systems, Applied Physics Letters 80, 908 (2002).
- [27] S. F. Koufidis and M. W. McCall, Möbius transformation and coupled-wave theory: Complete identification of the transfer matrix, Physical Review A 106, 062213 (2022).
- [28] L. Faddeev, How algebraic bethe ansatz works for integrable model, arXiv preprint hep-th/9605187 (1996).
- [29] B. Grammaticos, T. Tamizhmani, and Y. Kosmann-Schwarzbach, Discrete integrable systems, Discrete Integrable Systems 644 (2004).
- [30] J. B. Pendry, Low energy electron diffraction: the theory and its application to determination of surface structure, 2 (Academic Press, 1974).
- [31] C. E. J. Png and Y. Akimov, Nanophotonics and plasmonics: An integrated view, (2017).
- [32] U. Fano, Sullo spettro di assorbimento dei gas nobili presso il limite dello spettro d'arco, Il Nuovo Cimento (1924-1942) 12, 154 (1935).
- [33] I. Avrutsky, R. Gibson, J. Sears, G. Khitrova, H. Gibbs, and J. Hendrickson, Linear systems approach to describing and classifying fano resonances, Physical Review B 87, 125118 (2013).
- [34] J. Schwinger, L. L. DeRaad Jr, K. Milton, and W.-y. Tsai, Classical electrodynamics (Westview Press, 1998).
- [35] S.-W. Lee and R. Mittra, Fourier transform of a polygonal shape function and its application in electromagnetics, IEEE Transactions on Antennas and Propagation 31, 99 (1983).
- [36] J. Wuttke, Form factor (fourier shape transform) of polygon and polyhedron, arXiv preprint arXiv:1703.00255 (2017).
- [37] full-wave CST Microwave studio.
- [38] W. R. Inc., Mathematica, Version 11.3, champaign, IL, 2018
- [39] M. Barbuto, Z. Hamzavi-Zarghani, M. Longhi, A. Monti, D. Ramaccia, S. Vellucci, A. Toscano, and F. Bilotti, Metasurfaces 3.0: a new paradigm for enabling smart electromagnetic environments, IEEE Transactions on Antennas and Propagation (2021).
- [40] J. Zhou, P. Zhang, J. Han, L. Li, and Y. Huang, Metamaterials and metasurfaces for wireless power transfer and energy harvesting, Proceedings of the IEEE (2021).
- [41] H. A. Atwater and A. Polman, Plasmonics for improved

- photovoltaic devices, Nature materials 9, 205 (2010).
- [42] A. A. Eteng, H. H. Goh, S. K. A. Rahim, and A. Alomainy, A review of metasurfaces for microwave energy transmission and harvesting in wireless powered networks, IEEE Access 9, 27518 (2021).
- [43] D. Ferreira, R. F. Caldeirinha, I. Cuinas, and T. R. Fer-
- nandes, A review of manufacturing materials and production methods for frequency-selective structures [wireless corner], IEEE Antennas and Propagation Magazine **60**, 110 (2018).
- [44] J. Polo, T. Mackay, and A. Lakhtakia, *Electromagnetic surface waves: a modern perspective* (Newnes, 2013).